Accepted- The Journal of Physical Chemistry C

Ultra-Low-Temperature CO Oxidation Activity of Octahedral Site Cobalt Species in Co3O4 Based Catalysts: Unravelling the Origin of the Unique Catalytic Property

Tinku Baidya[a,*], Toru Murayama[b,*], Subramanian Nellaiappan[c], Nirmal Kumar Katiyar[d] Parthasarathi Bera[e], Olga Safonova[f], Mingyue Lin[b], Kaustubh R. Priolkar[g], Samapti Kundu[h], Bolla Srinivasa Rao[a], Patrick Steiger[f], Sudhanshu Sharma[c], Krishanu Biswas[d], Swapan Kumar Pradhan[h], N. Lingaiah[a], Masatake Haruta[b]

[a] Catalysis & Fine Chemicals Division, CSIR–Indian Institute of Chemical Technology, Hyderabad 500007, India

[b] Department of Applied Chemistry, Graduate School of Urban Environmental Sciences, Tokyo Metropolitan University, 1-1 Minami-Osawa, Hachioji, Tokyo 192-0397, Japan

[c] Department of Chemistry, Indian Institute of Technology Gandhinagar, Gujrat 382355, India

[d] Department of Materials Science and Engineering, Indian Institute of Technology Kanpur, Kanpur 208016, India

[e] Surface Engineering Division, CSIR–National Aerospace Laboratories, Bengaluru 560017, India

[f] Paul Scherrer Institut, 5253 Villigen, Switzerland

[g] Department of Physics, Goa University, Taleigao Plateau, Goa 403206, India

[h] Materials Science Division, Department of Physics, University of Burdwan, Golapbag, Burdwan 713104, India

Abstract

Co_3O_4 with spinel structure is known for unique CO oxidation activity at very low temperature under dry condition. In this study, five model spinel catalysts including $MnCo_2O_4$, $MnFe_2O_4$, $CoCr_2O_4$, $CoFe_2O_4$ and $FeCr_2O_4$ have been chosen to understand the active coordination site as well as the origin of unusual catalytic activity in Co_3O_4 based catalysts. The detailed analysis of bulk and crystal surface structure, basic nature of the surface and redox properties of the active metals have been performed to understand the unusual catalytic activity. While Mn occupies octahedral site in $MnCo_2O_4$ and $MnFe_2O_4$, both Co and Fe are equally distributed between octahedral and tetrahedral sites. On the other hand, $CoCr_2O_4$ contains Co and Cr in tetrahedral and octahedral sites, respectively. Low-temperature CO oxidation activity decreases in the following order: $MnCo_2O_4$ >> $MnFe_2O_4$ > $CoCr_2O_4$. It indicates that Co^{2+} species in tetrahedral

site (in $CoCr_2O_4$) remains inactive for low-temperature catalytic activity, while Co^{3+} in octahedral site (in $MnCo_2O_4$) is active in Co_3O_4 based catalysts. This result was corroborated with $CoFe_2O_4$, inverse spinel structure, showed higher activity than $CoCr_2O_4$. Fe, being a weak redox metal, does not show low-temperature activity, although, crystallite facets of $MnCo_2O_4$ and $MnFe_2O_4$ catalysts are predominantly exposed in (100) and (110) lattice planes, which contain similar concentration of Co^{3+} and Fe^{3+} species in both. Redox potential for CO oxidation involving Co^{3+}/Co^{2+} couple in $MnCo_2O_4$ indicates a highly favorable reaction, while a non-responsive behavior of Co species was observed in $CoCr_2O_4$. CO oxidation starting at –40 ^oC over $MnFe_2O_4$ and then a sluggish catalytic activity extended toward above 200 ^oC indicate that $Fe^{3+} \rightarrow Fe^{2+}$ step is favorable, but re-oxidation of Fe^{2+} could be difficult at low temperature. Both CO and H_2-TPR indicate much higher reducibility of Co species in $MnCo_2O_4$ as compared with Co species in $CoCr_2O_4$ or Fe in $MnFe_2O_4$.

***Corresponding authors:**

Email: tinku26@gmail.com ; baidya@iict.res.in ; murayama@tmu.ac.jp

1. Introduction

Ambient temperature CO oxidation is useful for in-door air quality control, purification of H_2 for fuel cells, pure N_2 and O_2 gas production from air in the semiconductor industry, gas sensing of CO traces and so forth.[1–4] CO oxidation at very low temperature (below 0 ^oC) has been an exciting topic in catalysis. The pioneering work of Haruta's group on supported Au has triggered tremendous interest in low-temperature CO oxidation.[5] Supported Au nanocluster catalysts have shown excellent activity below 0.0 ^oC.[6–10] However, cheaper alternative for this reaction is highly desirable. Some metal oxides, especially Co_3O_4, are also known to be active for CO oxidation at ambient temperature.[11–17] CO oxidation below even –50 ^oC over Co_3O_4 has

been intensively studied and varying activities (in term of T_{50}) have been reported depending on physical properties and reaction conditions.[18–25] The activity in Co_3O_4 is significantly enhanced by doping with various metal substituents like Fe, Bi, In etc, although these metals have hardly any role in redox reaction itself.[26–31] These few metal doped Co_3O_4 catalysts have shown T_{100} for CO oxidation at nearly –100 ^oC.

Several spectroscopic and theoretical studies have aimed at CO oxidation understanding reaction mechanism over Co_3O_4 based catalysts. While Polard et al. have found CO adsorption on Co^{2+} and forming CO_2 by combining with adjacent oxygen, all theoretical studies have claimed CO adsorption on Co^{3+} ion.[32–35] Theoretical studies also have looked into the role of low coordinated oxygen in Co_3O_4, have failed to give insight into unique catalytic behavior of Co^{3+} ion in spinel structure. Wang et al. have done a comprehensive calculation of energetics involving CO adsorption step to CO_2 formation on various oxide and surfaces.[36] However, the model reaction steps taken for calculation may not be the absolute reality. It's reasonable to assume that when a neutral molecule like CO (electron donor) gets adsorbed on a highly redox Co^{3+} (electron acceptor) metal site, there must be partial charge transfer and thereby CO molecule gets slightly positively charged. Therefore, negatively charged lattice oxygen may react with positively charged CO molecule at faster rate due to ionic interaction. Since these important steps find hard to be proved by normal spectroscopic methods and are missed in the grossly presented reaction steps for calculation, origin of unique catalytic property of Co^{3+} in Co_3O_4 structure still remains unsolved, requiring direct experimental evidence.

The paper also established reactivity order of the major planes as following: (110) > (100) > (111).[36] The difference of catalytic activities in different planes has been correlated to the concentration of Co^{3+} species and surrounding low-coordinated (two and three) oxygen atoms.

Co_3O_4 nanorods with predominantly exposed (110) faces have been found to exhibit very high activity for CO oxidation at −77 °C under normal conditions.[20] Teng et al have investigated the importance of crystal morphology.[25] They have found plate like Co_3O_4 with (111) planes more active as compared with cubic and rod shaped Co_3O_4 containing (100) and (110) planes, respectively. Even higher surface area of rod shaped catalyst compared to plate shaped one (62 vs 36 m^2g^{-1}) has made only minor difference in catalytic activity. Therefore, attribution of origin of low-temperature CO oxidation activity to Co^{3+} and low-coordinated oxygen species alone seems to be not enough to explain low-temperature activity. Therefore, there is something intrinsic in cobalt atom itself that makes it so unique in spinel structure.

In Co_3O_4, Co^{2+} and Co^{3+} respectively occupy the tetrahedral and octahedral coordination sites mainly. The substitution of Co^{3+} with non-redox Cr^{3+} ion substituent in octahedral site demonstrated gradually increasing T_{50} for CO oxidation with increasing concentration.[31] This trend has confirmed that Co^{3+} in octahedral site is responsible for low-temperature CO oxidation activities over Co_3O_4 based catalysts. As experiments have been carried out at very low temperature, lack of in-depth investigation into the reaction mechanism remains the big barrier to understanding. Although, theoretically, energetics of mechanism of CO oxidation with different model steps on a number of catalysts surfaces have been studied, effect of basicity, redox potential of active metals on the catalyst surface etc have not been studied before. In short, realistic model is missing for the low-temperature reaction and the question arises why Co^{3+} in octahedral site is so active.

In the present study, the origin of unusual activity of cobalt species toward CO oxidation at very low temperature at particular site along with reliable reference catalysts has been

investigated. Apart from crystallite surface planes and surface basicity, redox property in Co species has been investigated and correlated to the unique catalytic behavior.

2. Experimental details

$MnCo_2O_4$, $MnFe_2O_4$ and $CoCr_2O_4$, $CoFe_2O_4$ and $FeCr_2O_4$ were prepared by the solution combustion method using manganese nitrate ($Mn(NO_3)_2.xH_2O$, Sigma-Aldrich, 99.5%), cobalt nitrate ($Co(NO_3)_2.6H_2O$, Acros Organics, 99%), ferric nitrate ($Fe(NO_3)_3.9H_2O$, Sigma-Aldrich, 99.5%), and chromium nitrate ($Cr(NO_3)_3.9H_2O$, Alfa Aesar, 98.5%) as precursors using citric acid ($C_6H_8O_7$, Macron, 99%) as fuel. For the preparation of $MnCo_2O_4$, manganese nitrate, cobalt nitrate, and citric acid were taken in the ratio of 1.0:0.308:0.803 by weight. Similarly, for preparation of $MnFe_2O4$, $CoCr_2O_4$, $CoFe_2O_4$ and $FeCr_2O_4$ were also preparedusing corresponding element precursors together with fuel.The precursor compounds were dissolved in 30 mL of water in a 300 mL crystallizing dish resulting in a clear solution. The dish was then kept in a furnace preheated to 400 °C. The evaporation led to dehydration and then combustion with a flame started yielding the voluminous solid product within few minutes. Then, the solid product was grinded to fine powder and calcined in air at 400 ^oC for 3 h to remove residual carbon species.

The preparation of Co_3O_4 by above combustion technique produce low surface and less active material. Pure Co_3O_4 was prepared by decomposing Cobalt carbonate at 300 ^oC.

Nitrogen physisorption isotherms (adsorption–desorption branches) were measured on Quanta Chrome Autosorb Automated Gas Sorption System (Quantachrome Instruments) at 77 K. The samples were outgassed for 1 h under vacuum at 400 ^oC before measurement and the specific surface area (SSA) was determined using the Brunauer Emmett Teller (BET) method.

X-ray diffraction (XRD) patterns of the catalysts were obtained with an X-ray diffractometer (BRUKER D2 PHASER) equipped with a monochromator for CuK_α radiation at a voltage of 30 kV and a current of 100 mA. Fine powder samples were used for the XRD measurements and were scanned from 2θ = 20 to 100° at the rate of 0.02° s^{-1}. The observed diffraction patterns were identified using the International Centre for Diffraction Data (ICDD) database. XRD patterns of all the catalysts were analyzed using the Rietveld whole-profile fitting method based on structure and microstructure refinement.[37] The Rietveld software MAUD 2.26 was used to perform the simultaneous refinement of both material structure and microstructure using a least square refinement method.[38] All peaks were fitted with a pseudo-Voigt (pV) analytical function with asymmetry, as the pV function takes care of both the particle size and strain broadening of the experimental profiles. The background of each pattern was fitted by a polynomial of degree 5. In this method, Marquardt least-squares procedure was adopted for minimization of the difference between the observed (I_O) and simulated (I_C) intensities of XRD patterns. The minimization is monitored using the reliability index parameter, R_{wp} (weighted residue error), and R_{exp} (expected error) leading to the value of goodness of fit (GoF) as given below:[39]

$$\text{GoF} = \frac{R_{wp}}{R_{exp}}$$

The GoF value close to 1.0 indicates that the difference between observed and simulated intensities (I_o-I_c) approaches to zero and the fitting of the experimental XRD pattern with the refined simulated pattern turn gradually into accurate.

X-ray absorption spectra at Mn, Co, Fe and Cr K-edges were measured at SuperXAS beamline at the Swiss Light Source (Paul Scherrer Institute, Villigen, Switzerland) using the Si(111) channel cut monochromator. The rejection of higher harmonics and focusing were

achieved by a Si-coated collimating mirror at 2.8 mrad and a rhodium-coated toroidal mirror at 2.8 mrad, respectively. The size of the X-ray beam on the sample was 1.5 mm by 0.5 mm in horizontal and vertical directions, respectively, with a total intensity of about 5×10^{11} ph/s. The optimal amount of each sample was mixed with cellulose and pressed into pellets. The X-ray absorption spectra were measured in transmission mode using ionization chambers as the detectors. Reference foils of Mn (K-edge at 6539 eV), Co (K-edge at 7709 eV), Fe (K-edge at 7112 eV) and Cr (K-edge at 5989 eV) and were measured simultaneously with the samples for precise energy calibration. The spectra were reduced following the standard procedures in the Demeter program package.[40] Extended X-ray absorption fine structure (EXAFS) spectra in the range 3–14 $Å^{-1}$ were fitted in R-space between 1 and 3.5 Å using structural correlations obtained from their respective crystal structures.

For transmission electron microscopy (TEM), the material was dispersed in ethanol and few drops were deposited onto a perforated carbon foil supported on a copper grid. TEM investigations were performed on a CM30ST microscope (FEI; LaB6 cathode, operated at 300 kV, point resolution ~2 A).

The XPS of $MnCo_2O_4$, $MnFe_2O_4$ and $CoCr_2O_4$ catalysts were recorded using a Thermo Scientific Multilab 2000 spectrometer with non-monochromatic AlK_α radiation (1486.6 eV) as an X-ray source operated at 150 W (12.5 kV and 12 mA). The binding energies reported here were referenced with C 1s peak at 284.6 eV. All core level spectra were recorded with a pass energy and step increment of 40 and 0.05 eV, respectively. For XPS analysis, samples in the form of pellets of 8 mm diameter were mounted on the sample holders and placed into a preparation chamber with a vacuum of 8.0×10^{-8} mbar for 5 h in order to desorb any volatile species present on the surface. After 5 h, the samples were transferred into the analyzing

chamber with a vacuum of 5.0×10^{-10} mbar and the XPS data were recorded. The PeakFitv4.11 program was employed for curve-fitting of the Co 2p, Fe 2p, Cr 2p, and Mn 2p core level spectra into several components. The PeakFit v4.11 program was employed for the curve-fitting of the Fe 2p, Co 2p, Mn 2p Cr 2p and O 1s core level spectra into several components with Gaussian peaks after linear background subtraction. Peak positions, spin–orbit splitting, doublet intensity ratios, and full width at half maximum (FWHM) were fixed as given in the literature.

Temperature-programmed reduction (TPR) studies of the catalysts were performed with a Quantachrome Instrument (ChemBET-3000 TPR/TPD) to investigate their reduction behaviors. Typically, 25 mg of the sample was placed in a U-shaped quartz tube and ramped from 40 to 700 °C at 10 °C min^{-1} in a gas mixture containing 3% H_2/N_2. The consumption of H_2 during the reduction was monitored by a thermal conductivity detector (TCD). Prior to a TPR test, the sample was pretreated in oxygen gas flow at 400 °C for 15 min and then cooled down to room temperature in N_2 flow. The measurements for CO-TPR were carried out by using BELCAT II (MicrotracBEL). The catalyst (ca. 200 mg) was set into quartz reactor and pre-heated under 20 vol%O_2 /He (50 mL min^{-1}) at 400 ^oC for 1 h. Then temperature was down to -100°C and gas was switched to 5%CO/He (30 mL min^{-1}) flow for 30 min. The desorption profile from -100 to 700 ^oC was recorded with a mass spectrometer at a heating rate of 10 ^oC min^{-1} under 5%CO/He flow (30 mL min^{-1}). The decomposed gas molecules were monitored by a mass spectrometer (ANELVA, Quadrupole Mass Spectrometer, M-100QA, BEL Japan), collecting several mass fragments: CO_2 (44), CO(28), O_2 (32), H_2O (18).

The measurements for O_2-TPD were carried out by using BELCAT II (MicrotracBEL). The catalyst (ca. 50 mg) was set into quartz reactor and pre-heated under 20 vol%O_2 /He (50 mL min^{-1}) at 400 ^oC for 1 h. Then temperature was down to -100°C and gas was switched to He (30 mL

min^{-1}) flow for 30 min. The desorption profile from -100 to 700 ^oC was recorded with a mass spectrometer at a heating rate of 10 ^oC min^{-1} under helium flow (30 mL min^{-1}). The decomposed gas molecules were monitored by a mass spectrometer (ANELVA, Quadrupole Mass Spectrometer, M-100QA, BEL Japan), collecting several mass fragments: O_2 (32, 16), CO_2 (44), CO and N_2 (28), H_2O (18, 17, 16) and NH_3 (17, 16, 15).

CO_2-temperature programmed desorption (TPD) was conducted using a home built test set-up. Prior to the measurements, the samples were pelletized, crushed and sieved to the size fraction of 100–200 μm. Required amounts of sample were loaded into a tubular quartz reactor and sandwiched between two quartz wool plugs. A tubular furnace was used to provide heating. A K-type thermocouple centered inside the catalyst bed was used to record the temperature. Prior to CO_2 adsorption the catalyst was heated to 400 °C in N_2 and cooled down to room temperature (< 28 °C). This pretreatment was followed by 30 min saturation in 10 vol% CO_2 at room temperature before rinsing any excess CO_2 during 60 min of inert gas stream. The desorption experiments were conducted by ramping the temperature to 400 °C (5 °C min^{-1}) and simultaneously recording CO_2 concentration using a transmission infrared spectrometer (NICOLET ANTARIS IGS Analyzer, Thermo Scientific). Total flow rates were kept constant at 15000 mL h^{-1} g^{-1} for pretreatment as well as TPD.

Cyclovoltammetry (CV) studies were performed using the conventional three-electrode system at CHI660E electrochemical workstation. All solutions were prepared using double-distilled water. Working electrode was made by mixing 50 mg of catalyst and 100 μL of 5% Nafion solution as binder. After that 400 μL of isopropanol was added to it to make thin slurry followed by deposition on a glassy carbon (GC) electrode. Geometric area of the electrode was 0.071 cm^2. Platinum wire was used as the counter electrode, and Ag/AgCl electrode was used as

the reference electrode. The K_2SO_4 solution (0.5 M) was prepared and pH was adjusted to 6 using H_2SO_4, used as supporting electrolyte. For electrochemical oxidation of CO, the electrolyte was completely saturated with CO by purging for 30 min and CV experiments were performed on the various catalysts.

Catalytic activity was tested through CO oxidation reaction. The catalyst (0.15 g) was set in a fixed bed U-shaped reactor, and 1 vol% CO in air was flowed (50 mL min^{-1}). Reaction temperature was controlled by freezing mixture of liquid nitrogen and ethanol trap for lower than 0 ^oC, by water bath for temperatures from 0 ^oC to 80 ^oC, and by furnace for more than 100 ^oC. In the beginning, catalytic activity at room temperature were measured for 1 hour. Then, the reaction temperatures were changed from low temperature to high temperature step by step and kept for more than 20 min at each temperature. Finally, the catalytic activity at room temperature was checked again to confirm the deactivation. The reacted gas was analyzed at least 3 times at each temperature. The reacted gas was analyzed by micro-GC (Agilent 490) with MS5A (O_2, N_2, CO) and PoraPLOT Q (CO_2).

3. Results

The catalytic CO conversion vs temperature profiles for $CO + {}^1/_2O_2 \rightarrow CO_2$ reaction over AB_2O_4 type spinel catalysts including $MnCo_2O_4$, $CoCr_2O_4$, $CoFe_2O_4$, $FeCr_2O_4$ and $MnFe_2O_4$ along with parent Co_3O_4 are presented in Fig. 1. CO oxidation starts at ~ −75 ^oC, reaching T_{50} at −48 ^oC over Co_3O_4 catalyst. This catalyst has highest surface area and therefore, reaction has been carried out with normalized weight having equivalent surface area (See Table 1) with other catalysts mentioned above. Thus, T_{50} is reduced to −38 ^oC with normalized weight of Co_3O_4 catalyst. Interestingly, Co occupying different coordination site in $MnCo_2O_4$ and $CoCr_2O_4$ (see

EXAFS text later) demonstrates completely different catalytic activities, considering Mn and Cr as the non-redox entities in the above compounds, respectively. CO oxidation starts at ~100 ^{o}C over $CoCr_2O_4$ obtaining T_{50} at 180 ^{o}C. Gu et. al have also reported similar reactivity for $CoCr_2O_4$ catalyst.[41] Baidya et al. have also demonstrated that higher concentration of non-redox Cr^{3+} in octahedral site of Co_3O_4 gradually decreased the low-temperature CO oxidation activity.[31] This means tetrahedrally coordinated Co^{2+} species in $CoCr_2O_4$ cannot be responsible for low-temperature CO oxidation. Since Co atoms are distributed in both tetrahedral and octahedral sites, and tetrahedral Co^{2+} species are indicated inactivity for low-temperature CO oxidation, octahedral Co^{3+} species could be responsible for this unique activity in Co_3O_4. Interestingly, CO oxidation over $MnCo_2O_4$ starts at nearly –90 ^{o}C and reaches T_{50} at –65 ^{o}C. To see if the activity originates from the structure alone, $MnFe_2O_4$ has been chosen where Fe can also switch between +3 and +2 oxidation states like in Co ion. Interestingly, $MnFe_2O_4$ showed poor activity for CO oxidation with the reaction starting at –40 ^{o}C, but sluggishly increased to 100% conversion at ~240 ^{o}C. Other spinel based catalysts like $FeCr_2O_4$ and $CoFe_2O_4$ also have substantiated above results. As expectedly, $CoFe_2O_4$ shows higher activity than $MnFe_2O_4$ with T_{50} at 30 ^{o}C and $FeCr_2O_4$ shows least activity with T_{50} at 250 $^{\circ}$C. Above observation indicated that Co and Fe species make the difference in low-temperature CO oxidation activity between $MnCo_2O_4$ and $MnFe_2O_4$ oxides, and therefore, catalytic activities must be related to something concerning intrinsic redox nature. Therefore, efforts have been made for an in-depth analysis in the unique catalytic activity in the following sections.

The N_2 adsorption-desorption hysteresis curves for all catalysts are presented in Fig. 2. The BET surface area, pore diameter and volume are presented in Table 1. The surface areas of the catalysts ranges from 43 m^2g^{-1} to 127 m^2g^{-1}, having pore diameter and volume not

significantly different. It must be noted that $MnCo_2O_4$ showed the highest activity while it got the lowest surface area. This indicates that low temperature activity of Co_3O_4 based catalysts is related to some other property. The elemental compositions in the spinel compounds were analysed by ICP-AES method, showing almost desired ratio with deviation below 3% (see Table 1).

The XRD patterns have been Rietveld refined and the refined profiles of $MnFe_2O_4$, $MnCo_2O_4$, $CoCr_2O_4$ and $CoFe_2O_4$ are shown in Fig. 3. All the diffraction peaks match well with the face centered $MnFe_2O_4$ (JCPDF no. 10-0319; Sp.Gr. Fd-3m; cubic; a = 8.499Å), $MnCo_2O_4$ (JCPDF no. 23-1237; Sp.Gr. Fd-3m; cubic; a = 8.269Å), $CoCr_2O_4$ (JCPDF no. 78-0711, Sp. Gr. Fd-3m; cubic; a =8.334 Å) and $CoFe_2O_4$ (JCPDF no. 79-1744, Sp. Gr. Fd-3m; cubic; a =8.325 Å) with typical spinel (AB_2O_4) structures. However, Rietveld analysis reveals that cationic distributions in tetrahedral and octahedral sites of all these spinel compounds resemble well with the inverse spinel structure. In case of $MnFe_2O_4$, lattice parameter is refined from 8.499 Å to 8.347 Å. Similar trend is also observed in case of $MnCo_2O_4$ where lattice parameter is refined from 8.269 Å to 8.106 Å and for $CoCr_2O_4$ it is refined from 8.334 Å to 8.311 Å. Thus, in comparison to reported lattice parameter values, lattice contraction is noticed in all three compounds. It indicates that there are significant vacancies in these lattices. Different structural and micro/nano-structural parameters of $MnFe_2O_4$, $MnCo_2O_4$, $CoCr_2O_4$ and $CoFe_2O_4$ compounds as revealed from Rietveld refinement are summarized in Table S1.

Fig. S1 (a, b, and c) shows the structure model of inverse spinels $MnFe_2O_4$, $MnCo_2O_4$ and $CoCr_2O_4$, where all tetrahedral sites are occupied by Fe^{3+}, Co^{3+} and Cr^{3+} ions and octahedral sites are equally occupied by (Fe^{3+}, Mn^{2+}), (Co^{3+}, Mn^{2+}) and (Cr^{3+}, Co^{2+}) pair of cations respectively.

The presence of distortion and oxide vacancy could be corroborated by zero signal in Raman spectra of the catalyst, although, gross spinel structure remained intact in all catalysts (not presented here).

Fig. 4 shows X-ray absorption near edge structure (XANES) plots at the Co, Mn, Fe and Cr K-edges in Co_3O_4, $MnCo_2O_4$, $CoCr_2O_4$, and $MnFe_2O_4$. In Fig. 4(a), Co K-edges in Co_3O_4, $MnCo_2O_4$, and $CoCr_2O_4$ are plotted. XANES being sensitive to local site symmetry, site occupancy of metal ions in the above spinels can be speculated. For instance, a close similarity in XANES of Co in Co_3O_4 and $MnCo_2O_4$ indicates that Co ions occupy both tetrahedral and octahedral sites in $MnCo_2O_4$. This would imply that Mn ions primarily occupy octahedral sites in $MnCo_2O_4$. In comparison, the Co XANES in $CoCr_2O_4$ is quite different from that in Co_3O_4. These differences could be due to both, site occupancy as well as valence state. $CoCr_2O_4$ is known to be a normal spinel and hence it is expected that Co^{2+} ions occupy the tetrahedral sites. The identical positive shift in Co edge energy in Co_3O_4 and $MnCo_2O_4$ as compared to $CoCr_2O_4$ is then an indication of existence of Co^{2+} and Co^{3+} in Co_3O_4 and $MnCo_2O_4$. This would further imply that Mn in $MnCo_2O_4$ is primarily in +2 oxidation state and occupies the remaining octahedral sites. The similarities in Mn XANES in $MnCo_2O_4$ and $MnFe_2O_4$ are seen in Fig. 4(b) therefore point to octahedral site occupation of Mn in $MnFe_2O_4$ which would immediately imply Fe ions occupying both tetrahedral and octahedral sites. The Fe K-edge XANES in $MnFe_2O_4$ is presented in Fig. 4(c). The normal spinel nature of $CoCr_2O_4$ points to Cr ions occupying the octahedral sites. This is further substantiated with close similarity in the XANES features observed in Cr K-edge in $CoCr_2O_4$ (Fig. 4(d)) and Mn K-edges in $MnCo_2O_4$ and $MnFe_2O_4$ (Fig. 4(b)).

To further substantiate the site occupancy of different metal ions and understand their local structure, extended X-ray absorption fine structure (EXAFS) signals at the K-edges of Co, Mn, Fe, and Cr have been analyzed. Fig. 5(a) depicts magnitude of Fourier Transform (FT) of Co K-edge EXAFS in Co_3O_4. Three peak-like features centered at about 1.6 Å, 2.5 Å and 2.8 Å correspond to the nearest neighbor Co–O and next nearest neighbor Co–Co correlations. It may be noted that the FT spectra are not corrected for phase shift and hence the correlations appear at lower R values in the figure as compared to bond length values given in the Table 2. Co EXAFS in Co_3O_4 has been fitted with first three near neighbor correlations obtained for tetrahedral and octahedral sites. For this the structural model based on crystal structure of Co was constructed and the scattering paths with respect to these correlations were obtained using FEFF6.0. While fitting the tetrahedral and octahedral correlations have been multiplied by a constant factors corresponding to number of sites of each symmetry in the spinel structure. The fit is depicted by solid line in the Fig. 5(a) and the parameters obtained are given in Table 2. Similar fitting procedure was used in fitting EXAFS data at the Co K-edge and Mn K-edge in $MnCo_2O_4$, Mn K- and Fe K-edge in $MnFe_2O_4$ and Co K-edge and Cr K-edge in $CoCr_2O_4$. These data along with best fit lines are presented in Fig. 5(b), Fig. 6(a) and Fig. 6(b) respectively and the parameters are listed in Table 2. Accordingly, in $MnCo_2O_4$, Co ions occupy the tetrahedral and octahedral sites while Mn ions are majorly/only at octahedral positions. While in $CoCr_2O_4$, the octahedral sites are occupied only by Cr ions and the tetrahedral sites are occupied by Co ions as expected for a normal spinel. $MnFe_2O_4$, like $MnCo_2O_4$ is an inverse spinel with Fe atoms occupying both the tetrahedral and half of the octahedral sites. Rest of the octahedral sites are occupied by Mn ions. The structure of $CoFe_2O_4$ have been studied in the literature, indicating formation of a partially inverse spinel structure.[42]

The elemental distribution maps, crystallinity of the materials and surface morphologies of the crystallites have been analyzed by TEM studiies. Fig. 7 shows elemental maps in all spinels catalysts, indicating homogeneous distribution of respective elements in all compounds. Fig. 8 presents electron diffraction (ED) patterns in $MnCo_2O_4$, $MnFe_2O_4$, $CoCr_2O_4$ and $CoFe_2O_4$ showing pure spinel structure pattern and also confirm the absence of MnOx, FeOx and CrOx as separate phase in the compounds. The absence of diffused ring patterns also confirm absence of amorphous phase. Fig. 9 presents TEM images of representative $MnCo_2O_4$ and $MnFe_2O_4$ catalysts, respectively. The crystallite sizes ranged from 9 – 15 nm. By analyzing nearly 50 fringes at different spots in the images, approximate populations of crystallite planes have been calculated. The crystallite surfaces contain about 62% (311), 33% (022) and 5% of (044) in $MnCo_2O_4$ catalyst. On the other hand, approximately, 57% (022), 13% (311), 13% (222) and 17% (400) are found in $MnFe_2O_4$ catalyst. Obviously, (311) and (220) planes corresponding to respective d-spacing 0.25 and 0.29 nm are respectively found predominant in $MnCo_2O_4$ and $MnFe_2O_4$ catalysts. The fringes of (311), (220) and (111) lattice planes in the TEM are projected with (100), (110) and (1-10) lattice planes as shown in Fig. 10. Since Co^{3+} was considered to be active site, order of catalytic activity in different lattice planes can be determined based on Co^{3+} concentrations. A theoretical calculation has established that activation energies for CO oxidation on various crystal planes correlating catalytic activity to the concentration of Co^{3+} ions and low coordinated oxygen species.[36] It also showed that active surfaces can be terminated differently and resulting in varying activation barriers for the reaction. However, it's a fact that octahedral Co^{3+} is the only active site responsible for CO at very low temperature. Therefore, equal concentration of Co^{3+}/Fe^{3+} species in (100) and (110) surfaces (see Fig. 10) and their

different activities in $MnCo_2O_4$/$MnFe_2O_4$ indicates that catalytic activity is related to the nature of the respective metal ion itself.

Detailed XPS studies of $MnCo_2O_4$, $CoCr_2O_4$, $MnFe_2O_4$ and $CoFe_2O_4$, and $FeCr_2O_4$ catalysts can provide very useful information about the elemental oxidation states of the catalysts. The binding energy and relative peak area related to all elements are presented in Table 3. Broad Mn2p core level spectra in $MnCo_2O_4$ and $MnFe_2O_4$ catalysts indicate the presence of Mn in multiple oxidation states that can be curve-fitted into component peaks. Curve-fitted Mn $2p_{3/2,1/2}$ core level spectra of $MnCo_2O_4$ and $MnFe_2O_4$ are presented in Fig. 11. Intense Mn $2p_{3/2,1/2}$ peaks around 640.8 and 652. eV with 11.4 eV spin-orbit separation in $MnCo_2O_4$ correspond to Mn^{2+} species in these types catalysts.[43,44] A weak shake-up satellite peak observed at 646.4 eV confirms the presence of Mn^{2+} species in the catalysts. Other spin-orbit component peaks at 643.2 and 654.6 eV are assigned for Mn^{4+} species. Surface concentrations of Mn^{2+} species in $MnCo_2O_4$ and $MnFe_2O_4$ are 70% and 56%, respectively, whereas remaining amounts in both cases are related to Mn^{4+} species. Spectral nature of Co2p core level of $MnCo_2O_4$ catalyst is broad which indicates that Co is present in different oxidation states and spectra are curve-fitted into sets of spin-orbit doublets along with associated satellite peaks. Curve-fitted Co 2p core level spectrum of $MnCo_2O_4$ is shown in Fig. 12. Co $2p_{3/2,1/2}$ peaks at 779.7 and 794.8 eV with spin-orbit separation of 15.1 eV is assigned for Co^{3+}, whereas peaks at 781.8 and 796.8 eV with 15.0 eV spin-orbit separation are related to Co^{2+} species.[31,45] It has been in the literature that binding energy peaks associated with oxidized Co $2p_{3/2,1/2}$ species are located at 780.5 ± 1.5 and 796.0 ± 1.5 eV, respectively. Earlier studies have demonstrated that differences in the 2p peak positions between Co^{2+} and Co^{3+} vary from 0.1 to 1.5 eV making it difficult to use the primary 2p peaks for distinguishing between Co^{2+} and Co^{3+}. However, Co 2p core level spectra of these

two oxides can be distinguished by the differences in their satellite features. The Co 2p spectrum of Co^{2+} contains prominent satellite peaks with 4–6 eV higher binding energy than the primary peaks. In contrast, Co^{3+} species is recognized by the presence of weak satellite peaks at 9 – 10 eV higher binding energy than the main peaks. In the $MnCo_2O_4$ catalyst, the Co $2p_{3/2}$ peak around 779.7 eV along with the satellite peak at 789.5 eV corresponds to Co^{3+} species, whereas the $2p_{3/2}$ peak at 781.8 eV with the satellite peak at 786.1 eV is assigned for Co^{2+} species. These satellite features arise from shake-up phenomenon in which the excitation of unpaired valence electrons increases the number of relaxed final states. Surface concentrations of Co^{2+} and Co^{3+} in $MnCo_2O_4$ catalyst are 29 and 71%, respectively. On the other hand, Co is in completely +2 oxidation state in $CoCr_2O_4$ catalyst as Co $2p_{3/2,1/2}$ spin-orbit peaks are observed at 781.1 and 796.4 eV along with characteristic satellite peaks. XPS of curve-fitted Fe 2p and Cr 2p core levels in $MnFe_2O_4$ and $CoCr_2O_4$ catalysts are presented in Fig. 13. Fe 2p core level spectrum is observed to be broad in nature and is curve-fitted into several Fe species. Fe $2p_{3/2,1/2}$ peaks observed at 709.5 and 723.4 eV in Fig. 13(a) are assigned for Fe^{2+} species present in the catalyst and $2p_{3/2,1/2}$ peaks at 711.5 and 725.4 eV are attributed to Fe^{3+} species, respectively.[31] Fe^{2+} and Fe^{3+} species in Fe2p core level spectra are distinguished by their respective satellite peak positions. According to the literature, in Fe 2p core level spectrum of Fe^{2+} species, intense satellite peaks are observed around 4.5–5.5 eV above the main peaks and weak satellite peaks associated with Fe^{3+} species are found around 7–9 eV above the main peaks. In Fig. 13(a), presence of satellite peaks at higher binding energies confirms the presence of Fe^{3+} in the catalyst. Surface concentrations of Fe^{2+} and Fe^{3+} species are 40 and 60%, respectively. Observed Cr 2p core level spectrum in $CoCr_2O_4$ is broad in character indicating the presence of different Cr species in the catalyst which is decomposed into component peaks by curve-fitting. In Fig.

13(b), Cr $2p_{3/2,1/2}$ peaks found at 576.2 and 585.8 eV with 9.6 eV spin-orbit separation is attributed to Cr^{3+} species.[31] Low intense component peaks at 578.7 and 588.5 eV with 9.8 eV spin-orbit separation corresponds to either Cr^{3+} species in $Cr(OH)_3$ or Cr^{6+} species.[46,47] Formation of hydroxide species may be more plausible as component peak associated with hydroxide species is found in O 1s core level spectrum (discussed later). However, it is evident from XPS studies that Cr^{3+} species are the dominant species in the $CoCr_2O_4$ catalyst. XPS of studies demonstrate that Fe is in +2 and +3 oxidation states in $CoFe_2O_4$ and $FeCr_2O_4$ and Co and Cr are observed to be in +2 and +3 oxidation state, respectively (See Fig. S2 and Fig. S3). XPS of O 1s core levels of $MnCo_2O_4$, $MnFe_2O_4$ and $CoCr_2O_4$ catalysts have also been performed. Broad spectral envelopes of O 1s core levels indicate the presence of different oxygen species in the catalysts and are resolved into component peaks by curve fitting. Typical curve-fitted O 1s core level spectra of $MnCo_2O_4$, $MnFe_2O_4$ and $CoCr_2O_4$ catalysts are shown in Fig. 14. Decomposed peak at 530.0 eV is attributed to lattice oxide species (O^{2-}) and peaks around 531.6 and 533.4 eV correspond to hydroxyl and adsorbed water species, respectively present in the catalysts (see Table S2 also). However, oxide species is the major component species in relation with other two species in all the catalysts.

The redox properties of the catalytic materials were investigated by both H_2- and CO-TPR studies. Fig. 15(a) presents H_2-TPR profiles of Co_3O_4, $MnCo_2O_4$, $MnFe_2O_4$ and $CoCr_2O_4$ catalysts. The two-step reduction of Co species in Co_3O_4 is distinguished with a clear valley 375 ^oC. It includes two consecutive steps: Co^{3+} (Co_3O_4) $\rightarrow$ Co^{2+} (CoO) below 375 ^oC and CoO $\rightarrow$ Co (metal) above this temperature. The redox reaction on the surface determines the catalytic activity, therefore, hydrogen uptake corresponding to the low-temperature peak is discussed rather than exploring bulk reduction. The low-intensity reduction in Co_3O_4 starting from 90 ^oC

and extending up to 215 ^{o}C indicates the presence of active redox sites on the surface, while sub-surface to bulk reduction starts above 215 ^{o}C leading to complete reduction below 500 ^{o}C. By looking at TPR profile of $MnCo_2O_4$, one can realize that reduction of mainly Co species is responsible two peaks, like in Co_3O_4. In this case, surface reduction starts at 115 ^{o}C following sub-surfaces and bulk ending total reduction below 675 ^{o}C. The low-temperature peak is not shifted by the presence of Mn in Co_3O_4, but, it pushed the high temperature peak toward higher temperature from 440 ^{o}C to 545 ^{o}C. A new peak appears as shoulder on the left side of the low-temperature peak (marked by *) at 287 ^{o}C, which could be due to partly reduction of Mn^{4+} as indicated by XPS before. The TPR profile of $MnFe_2O_4$ indicates a weak redox catalyst in comparison with above ones. The intensity of low-temperature peak, which starts at 150 ^{o}C, is significantly diminished and also the higher temperature reduction extended to above 700 ^{o}C. To determine the reduction at low-temperature in $MnCo_2O_4$, a comparison with $MnFe_2O_4$ could be useful considering similar size and oxidation states of Co and Fe. The low-temperature peak indicates only 39% is reduced in $MnFe_2O_4$ as compared with $MnCo_2O_4$ that involved $Co^{3+} \leftrightarrow Co^{2+}$ or $Fe^{3+} \leftrightarrow Fe^{2+}$ couples. Since Mn^{2+} is considered to be non-reducible under this condition, reduction of Co^{3+} or Fe^{3+} in $MnCo_2O_4$ and $MnFe_2O_4$ catalysts must be related to intrinsic reduction potential of the metal ions in the compounds. This temperature shifts indicate that Co^{3+} is stronger oxidant as compared with Fe^{3+}. The low temperature peak in $CoCr_2O_4$ could be due to reduction of higher valent Cr species as indicated in XPS before.

Fig. 15(b) shows CO-TPR in the above catalysts. Clearly, CO_2 formation is observed at as low as –80 ^{o}C over $MnCo_2O_4$ and at 40 ^{o}C over $MnFe_2O_4$. The reduction at highest temperature in $CoCr_2O_4$ indicated least reactivity of Co^{2+} and Cr^{3+} for low temperature reaction. These results were expected as it is observed in CO oxidation above. However, there was a clear difference in

reactivity with CO and H_2 as reductants, originating from different nature of adsorption. CO is easily adsorbed on transition metal ion like Co^{3+} due to synergistic electronic effect through π-bond formation as compared with H_2 adsorption through σ bond donation.

To understand CO oxidation activity in the catalysts, desorption behavior of reactant O_2 (especially) and acidic CO_2 product were extremely important. Figure 16a shows O_2 TPD profiles in $MnCo_2O_4$, $MnFe_2O_4$, and $CoCr_2O_4$ catalysts. The profiles unravel the existence of two types of oxygen species in the catalysts – weakly bound oxygen species desorbing below 300 ^oC and strongly bound/bulk oxygen species desorbing above 300 ^oC. The desorption starts at 50 ^oC and 90 ^oC from $MnCo_2O_4$ $MnFe_2O_4$, respectively, peaking around 130 ^oC. The peak area below 300 ^oC comes in the order as following: $CoCr_2O_4 < MnFe_2O_4 << MnCo_2O_4$. This indicates that weakly bound oxygen exist abundantly in $MnCo_2O_4$ as compared with $MnFe_2O_4$. As expectedly, $CoCr_2O_4$ do not show any weakly bound oxygen species in the surface.

The desorption of product CO_2 can play a very important role in availing the active site, depending on strength and amount of adsorbed CO_2. Fig. 16b shows CO_2-TPD profiles for $MnCo_2O_4$, $MnFe_2O_4$, and $CoCr_2O_4$ catalysts. While $MnCo_2O_4$ and $MnFe_2O_4$ show CO_2 desorption, $CoCr_2O_4$ surface indicates absence of adsorbed CO_2. The desorption starts at 25 ^oC and peaking at ~ 70 ^oC in both $MnCo_2O_4$ and $MnFe_2O_4$ catalysts. Desorption at low temperature indicates that CO_2 is weakly attached to the surface. Clearly, CO_2 desorption is 4.5 times higher over $MnCo_2O_4$ as compared with $MnFe_2O_4$ catalyst. Therefore, as CO oxidation occurs at much low temperature over $MnCo_2O_4$ as compared with $MnFe_2O_4$ or $CoCr_2O_4$, weakly interacting CO_2 does not have any effect on large variation in temperature CO oxidation.

In order to understand the reaction behavior observed in the gas solid reaction, electrochemical experiments have also been performed both in pure electrolyte solution as well

as electrolyte saturated with CO. The CV behaviors in pure electrolyte at two different scan rates are shown in Fig. 17. At both the scan rates, CV with $CoCr_2O_4$ (Fig. 17(a)) looks featureless stating that redox reactions on the surface are absent. It means both Co^{2+} and Cr^{3+} remains inactive during redox reactions on the surface of this catalyst and therefore, one does not see any redox peak in the CV.

Between $MnCo_2O_4$ and $MnFe_2O_4$ catalysts, presence of Fe and Co make the difference in similar structure and therefore, CV behavior may relate to their respective redox properties. The curve for $MnCo_2O_4$ catalyst as shown in Fig. 17(b) is a typical of a resistive system. At 40 mV s^{-1}, there appear broad features in the CV but it is hard to understand the processes involved. At 20 mV s^{-1}, some redox reactions are noticed. Specifically, peaks at 0.7 and 1.1 V appear in the oxidation scan and in the reverse scan the peaks appear at 0.7 and 0.1 V. Since Co^{2+} in tetrahedral site is inactive, these peaks are related to Co species in octahedral site and is known to be redox active.[48] As per the E-pH diagram, the specific reaction occurring in the CV are related to $CoO(OH)/Co^{2+}$ redox couple. In this reaction, oxidation state of cobalt changes from +3 to +2.

Opposite to this observation, CV of $MnFe_2O_4$ shows well defined peaks at 1.1 V in the oxidation cycle and its subsequent reduction in the reverse scan at 0.9 V (Fig. 17c) at both the scan rates. These peaks are different from $MnCo_2O_4$ and therefore, appear due to the presence of Fe as they do not appear in other systems consisting of no Fe. Other peaks at 0.42 V in oxidation scan and 0.4 V in reduction scan are assumed to be for surface oxidation by water / hydroxide as they appear quite on top of each other. Surface oxidation and reduction peak should also be present in other catalysts but are probably masked by the nature of the CV.

Electrochemical CO oxidation is a useful way to assess the active sites present on the surface. The shape and area under the curve can give information about the active sites present in the material. Usually, CO which is adsorbed on the catalyst's surface is oxidized with the help of hydroxyls as shown in the following reaction: $CO + 2OH^- \rightarrow CO_2 + H_2O$.CV before and after CO saturated electrolyte at the scan rate of 20 mV s^{-1} for the above catalysts are shown in Fig. 16. In $CoCr_2O_4$, post CO saturation overall current of the CV as shown in Fig. 18(a) has decreased. This explains that CO has a poisoning effect on the catalyst surface. This effect has usually been noticed in the hydrogen adsorption region on Pt nanoparticles.[49] Similarly, CV, before and after the CO saturation on $MnCo_2O_4$ is shown in Fig. 18(b). Noticeably, a significant peak due to CO oxidation appears with an onset voltage of 0.94 V and the peak voltage of 1.15 V. Peak is slightly broad in comparison to the well-defined Pt surfaces[50] explaining that the active sites are heterogeneous in nature such as in alloys or supported catalysts.[51,52] Moreover, the adsorption strength is optimum resulting in high activity. This result correlates well with the gaseous oxidation of CO in presence of O_2. Other than the CO oxidation, two peaks with significant intensity are observed in the reverse scan at 0.85 and 0.2 V. These peaks are due to the reduction of the product forming in the oxidation cycle, i.e. CO_2.

Electrochemical oxidation of CO on $MnFe_2O_4$ is shown in Fig. 18c. After CO saturation in the electrolyte, oxidation peak with an onset voltage of 0.97 V is noticed with much smaller intensity compared to $MnCo_2O_4$. Onset voltage is 300 mV higher than $MnCo_2O_4$ indicating high activation energy or sluggish kinetics for CO oxidation in the case of $MnFe_2O_4$.

4. Discussion

Co_3O_4 is known for CO oxidation activity at very low temperature and this study was aimed to understand the origin of the unique catalytic property. Bulk structure and crystallite surface

properties have been analyzed and then redox property has been investigated that correlates well with observed catalytic property. Parent Co_3O_4 oxide has two types of Co species in the lattice – tetrahedral and octahedral coordinated species. It is required to distinguish the active site/atom among these sites. By blocking Co^{3+} in octahedral site with non-redox Cr^{3+} in Cr/Co_3O_4 catalysts, catalytic activity has been found to decrease gradually with increasing concentration of Cr. Since Co^{2+} in tetrahedral site remains inactive for low-temperature catalytic activity, Co^{3+} in octahedral site must be the active site. To see uniqueness of octahedral Co species in spinel structure, a similar type redox metal Fe (in $MnFe_2O_4$) has also been chosen, but it does not show low-temperature activity. Although, several theoretical studies have tried to give insight into reaction mechanism, there is no explicit evidence in support of unique catalytic activity of cobalt in spinel structure - whether it's structurally motivated or the intrinsic redox property of cobalt atom itself. The theoretical study of mechanism, without kinetics data as well as detailed spectroscopic studies, may be far from the reality. The energy minimization with certain configurations of reaction steps could be a crude approximation. Therefore, it is difficult to find reason behind the unique catalytic property of Cobalt species.

To look into possible factors, three Co_3O_4 based model catalysts such as $MnCo_2O_4$, $MnFe_2O_4$ and $CoCr_2O_4$ have been chosen, so that a fair comparison could be made by focusing on a particular redox site/species. These oxide catalysts are structurally similar. CO oxidation occurs at highest temperature over $CoCr_2O_4$ among these catalysts In this catalyst, Co remains exclusively in +2 state and occupying the tetrahedral site. The octahedral Cr^{3+} is a non-redox entity, so hardly takes part in reaction. This means that Co^{2+} in tetrahedral site cannot be the active species for low-temperature reaction in Co_3O_4 based catalysts. Mn occupies octahedral site in both $MnCo_2O_4$ and $MnFe_2O_4$ and therefore, Co and Fe are equally distributed in

tetrahedral and octahedral sites in the respective catalysts. Since Mn species is common in both $MnCo_2O_4$ and $MnFe_2O_4$ and $MnFe_2O_4$ demonstrated poor catalytic activity, octahedral Co^{3+} must be the active species for ultra low-temperature CO oxidation in $MnCo_2O_4$. Although, both Co and Fe can switch between +2 and +3 oxidation states, but there is huge difference in catalytic activities in terms of temperature. Thus, their activity for CO oxidation must be related to the intrinsic redox property of the respective elements.

This means structural feature fails to give reliable answer to the unique activity, and therefore, redox potential of the couples during CO oxidation could be playing important role. Intense peak in the electrochemical CO oxidation reaction with $MnCo_2O_4$ as compared to other model catalysts indicates the unique nature of Co species in octahedral site. On the contrary, a featureless CV for $CoCr_2O_4$ confirms that tetrahedral Co^{2+} cannot take part in redox reactions. A probable explanation with models is presented in Fig. 19. Co^{3+} in octahedral site can easily go to Co^{2+} state by reducing coordinated oxygen and then replenish the vacant site with oxygen by turning into Co^{3+} again (see Fig. 19a). On the other hand, Co^{2+} in tetrahedral site cannot go to higher oxidation state as it will require new oxygen for charge balance and need high energy to disturb the symmetry (see Fig. 19b).

The trend in redox properties was also supported by H_2-TPR and O_2 TPD results, exposing stark contrast between Co^{3+} and Fe^{3+} in their reduction behaviours. Reduction of surface at low temperature in $MnCo_2O_4$ is perfectly corroborated with desorption of O_2 at low temperature. Obviously, intensity of O_2 desorption related to weakly bound oxygen in $MnCo_2O_4$ was significantly higher than in $MnFe_2O_4$. This indicates that high redox power of Co^{3+} in octahedral site of Co_3O_4 based catalysts could be responsible for unusual catalytic property.

5. Conclusions

The investigation detected the active cobalt species and the origin of unusual catalytic activity of cobalt species in Co_3O_4 based catalysts. While Cobalt species in octahedral site was found to be active species, the tetrahedral site Co remained inactive. Huge redox peak obtained in CV indicated that high reduction potential of Co^{3+}/Co^{2+} couple in $MnCo_2O_4$ can be correlated to the unique CO oxidation activity of octahedral Co species at very low temperature. This was substantiated by no redox peak for CO oxidation with tetrahedral Co^{2+} species in $CoCr_2O_4$. The sluggish CO oxidation activity over $MnFe_2O_4$ starting from –40 ^oC and ending up at higher temperature indicated that irreversibility of redox cycle in Fe species at very low temperature. This study confirmed that Co^{3+}/Co^{2+} is unique unlike other redox couple like Fe^{3+}/Fe^{2+} couple. TPR and O_2 TPD studies together indicated presence of reactive oxygen species in MnCo2O4 catalyst, which could be due to strong redox ability of Co^{3+}/Co^{2+}.

Acknowledgement

N.K and K.B would like to thank Advanced Imaging Centre at IIT Kanpur for providing necessary software facilities for HRTEM data analysis.

References

1. Nero, A.; V, Jr. Controlling Indoor Air Pollution. *Sci. Am.* **1988**, *258*, 42 - 48.
2. Oh, S. E.; Sinkevitch, R.M. Carbon Monoxide Removal from H_2-Rich Fuel Cell Feed streams by Selective Catalytic Oxidation. *J. Catal.* **1993**, *142*, 254 - 262.
3. Thorogood, R. M.; Kleinberg, W. T. Inert Gas Purifier for Bulk Nitrogen Without the Use of Hydrogen or other Reducing Gases. US Patent 4869883 A (1989).

4. Funasaki, N.; Henmi, A.; Ito, S.; Asano, Y.; Yamashita, S.; Kobayashi, T.; Haruta, M. Development of Carbon Monoxide Detector Using Au Fine Particles-doped α-Fe_2O_3. *Sensor. Actuat. B: Chem.* **1993**, *14*, 536 - 538.
5. Haruta, M.; Kobayashi, T.; Sano, H.; Yamada, N. Novel Gold Catalysts for the Oxidation of Carbon Monoxide at a Temperature far Below 0 °C. *Chem. Lett.* **1987**, 405–408.
6. Vogel, W.; Cunningham, D. A. H.; Tanaka, K.; Haruta, M. Structural analysis of Au/$Mg(OH)_2$ during deactivation by Debye function analysis. *Catal. Lett*. **1996**, *40*, 175 - 181.
7. Cunningham, D. A. H.; Vogel, W.; Kageyama, H.; Tsubota, S.; Haruta, M. The Relationship between the Structure and Activity of Nanometer Size Gold When Supported on $Mg(OH)_2$. *J. Catal.* **1998**, *177*, 1 - 10.
8. Cunningham, D. A. H.; Vogel, W.; Haruta, M. *Catal. Let* Negative activation energies in CO oxidation over an icosahedral Au/$Mg(OH)_2$ catalyst. **1999**, *63*, 43 - 47.
9. Jia, C.-J.; Liu, Y.; Bongard, H.; Schüth, F. Very Low Temperature CO Oxidation over Colloidally Deposited Gold Nanoparticles on $Mg(OH)_2$ and MgO. *J. Am. Chem. Soc.* **2010**, *132*, 1520 - 1522.
10. Yoshida, T.; Murayama, T.; Sakaguchi, N.; Okumura, M.; Ishida, T.; Haruta, M. Carbon Monoxide Oxidation by Polyoxometalate-Supported Gold Nanoparticulate Catalysts: Activity, Stability, and Temperature-Dependent Activation Properties. *Angew. Chem.* **2018**, *130*, 1539 - 1543.
11. Teng, Y.; Sakurai, H.; Ueda, A.; Kobayashi, T. Oxidative removal of co contained in hydrogen by using metal oxide catalysts. *Int. J. Hydrogen Energy* **1999**, *24*, 355 - 358.
12. Njagi, E. C.; Chen, C.-H.; Genuino, H.; Galindo, H.; Huang, H.; Suib, S. L. Total Oxidation of CO at Ambient Temperature Using Copper Manganese Oxide Catalysts Prepared by a Redox Method. *Appl. Catal., B* **2010**, *99*, 103 - 110.

13. Jansson, J. Low-Temperature CO Oxidation over Co_3O_4/Al_2O_3. *J. Catal*. **2000**, *194*, 55 - 60.
14. Jansson, J.; Palmqvist, A. E. C.; Fridell, E.; Skoglundh, M.; Osterlund, L.; Thormahlen, P.; Langer, V. the Catalytic Activity of Co_3O_4 in Low-Temperature CO Oxidation. *J. Catal*. **2002**, *211*, 387 - 397.
15. Grillo, F.; Natile, M. M.; Glisenti, A. Low Temperature Oxidation of Carbon Monoxide: The Influence of Water and Oxygen on the Reactivity of a Co_3O_4 Powder Surface. *Appl. Catal., B* **2004**, *48*, 267 - 274.
16. Tüysüz, H.; Comotti, M.; Schüth, F. Ordered Mesoporous Co_3O_4 as Highly Active Catalyst for Low Temperature CO-oxidation. *Chem. Commun.* **2008**, 4022 - 4024.
17. Xu, C.; Liu, Y.; Zhou, C.; Wang, L.; Geng, H.; Ding, Y. An In Situ Dealloying and Oxidation Route to Co_3O_4 Nanosheets and Their Ambient-Temperature CO Oxidation Activity. *ChemCatChem* **2011**, *3*, 399 - 407.
18. Cunningham, D. A. H.; Kobayashi, T.; Kamijo, N.; Haruta, M. Influence of Dry Operating Conditions: Observation of Oscillations and Low Temperature CO Oxidation over Co_3O_4 and Au/Co_3O_4 Catalysts. *Catal. Lett.* **1994**, *25*, 257 - 264.
19. Haruta, M.; Yoshizaki, M.; Cunningham, D.A.H.; Iwasaki, T. Catalysis Research by Use of Ultra Pure Gas: Effect of Trace Amount of Water. *Ultra Clean Technol.* **1996**, *8*, 117 - 120 (in Japanese).
20. Thormahlen, P.; Skoglundh, M.; Fridell, E.; Andersson, B. Low-Temperature CO Oxidation over Platinum and Cobalt Oxide Catalysts. *J. Catal.* **1999**, *188*, 300 - 310.
21. Xie, X. W.; Li, Y.; Liu, Z. Q.; Haruta, M.; Shen, W. J. Low-Temperature Oxidation of CO Catalysed by Co_3O_4 Nanorods. *Nature* **2009**, *458*, 746 - 749.

22. Yu, Y.; Takei, T.; Ohashi, H.; He, H.; Zhang, X.; Haruta, M. Pretreatments of Co_3O_4 at Moderate Temperature for CO Oxidation at −80 °C. *J. Catal*. **2009**, *267*, 121 - 128.
23. Feng, Y. J.; Li, L.; Niua, S.; Qua, Y.; Zhang, Q.; Li, Y.; Zhao, W.; Li, H.; Shi, J. Controlled Synthesis of Highly Active Mesoporous Co_3O_4 Polycrystals for Low Temperature CO Oxidation. *Appl. Catal., B.* **2012**, *111−112*, 461 - 466.
24. Pandey, A. D.; Jia, C.; Schmidt, W.; Leoni, M.; Schwickardi, M.; Schüth, F.; Weidenthaler, C. Size-Controlled Synthesis and Microstructure Investigation of Co_3O_4 Nanoparticles for Low-Temperature CO Oxidation. *J. Phys. Chem. C* **2012**, *116*, 19405 - 19412.
25. Teng, Y.; Kusano, Y.; Azuma, M.; Haruta, M.; Shimakawa, Y. Morphology Effects of Co_3O_4 Nanocrystals Catalyzing CO Oxidation in a Dry Reactant Gas Stream. *Catal. Sci. Technol*. **2011**, *1*, 920 - 922.
26. Li, J.; Lu, G.; Wu, G.; Mao D.; Guo, Y.; Wang, Y.; Guo Y. The Role of Iron Oxide in the Highly Effective Fe-Modified Co_3O_4 Catalyst for Low-Temperature CO Oxidation. *RSC Advances* **2013**, *3*, 12409 - 12416.
27. Li, G.; Li, L.; Li, Y.; Shi J. A highly Moisture-Resistant Fe-doped Mesoporous Co_3O_4 Catalyst for Efficient Low-Temperature CO Oxidation. *New J. Chem.* **2015**, *39*, 1742 - 1748.
28. Lou, Y.; Ma, J.; Cao, X.; Wang, L.; Dai, Q.; Zhao, Z.; Cai, Y.; Zhan, W.; Guo, Y.; Hu, P.; Lu, G.; Guo, Y. Promoting Effects of In_2O_3 on Co_3O_4 for CO Oxidation: Tuning O_2 Activation and CO Adsorption Strength Simultaneously. *ACS Catal.* **2014**, *4*, 4143 - 4152.

29. Lou, Y.; Wang, L.; Zhao, Z.; Zhang, Y.; Zhang, Z.; Lu, G.; Guo, Y.; Guo, Y. Low-Temperature CO Oxidation over Co_3O_4-Based Catalysts: Significant Promoting Effect of Bi_2O_3 on Co_3O_4 Catalyst. *Appl. Catal., B* **2014**, *146*, 43 - 49.
30. Lou, Y.; Wang, L.; Zhang, Y.; Zhao, Z.; Zhang, Z. Lu, G.; Guo, Y. The effects of Bi_2O_3 on the CO oxidation over Co_3O_4. Catal. Today **2011**, *175*, 610 – 614.
31. Baidya, T.; Murayama, T.; Bera, P.; Safonova, O. V.; Steiger, P.; Katiyar, N. K.; Biswas, K.; Haruta, M. Low-temperature CO oxidation over combustion made Fe and Cr doped Co_3O_4 catalysts: Role of dopant's nature toward achieving superior catalytic activity and stability. *J. Phys. Chem. C* **2017**, *121*, 15256 - 15265.
32. Pollard, M. J.; Weinstock, B. A.; Bitterwolf, T. E.; Griffiths, P. R.; Newbery, A. P.; Paine III, J. B. A mechanistic study of the low-temperature conversion of carbon monoxide to carbon dioxide over a cobalt oxide catalyst. *J. Catal*. **2008**, *254*, 218 - 225.
33. Broqvist, P.; Panas, I.; Persson, H. A. A DFT Study on CO Oxidation over Co_3O_4. *J. Catal*. **2002**, *210*, 198 - 206.
34. Xu, X.-L.; Yang, E.; Li, J.-Q.; Chen, W.-K. A DFT Study of CO Catalytic Oxidation by N_2O or O_2 on the Co_3O_4(110) Surface. *ChemCatChem* 2009, *1*, 384 - 392.
35. Jiang, D.-E.; Dai, S. The role of Low-Coordinate Oxygen on Co_3O_4(110) in Catalytic CO Oxidation. *Phys. Chem. Chem. Phys.* **2011**, *13*, 978 - 984.
36. Wang, H.-F.; Kavanagh, R.; Guo, Y.-L.; Guo, Y.; Lu, G.; Hu, P. Origin of extraordinarily high catalytic activity of Co_3O_4 and its morphological chemistry for CO oxidation at low temperature. *J. Catal.* **2012**, *296*, 110 - 119.
37. Rietveld, H. M. Line profiles of neutron powder-diffraction peaks for structure refinement. *Acta Crystallogr*. **1967**, *22*, 151 - 152.

38. Lutterotti, L. *Maud Version 2.26*, http://www.ing.unitn.it/~maud/

39. Young, R.; Willes, A. D. B. Profile shape functions in Rietveld refinements**.** *J. Appl. Crystallogr.* **1982**, *15*, 430 - 438.

40. Ravel, B.; Newville, M. *ATHENA, ARTEMIS, HEPHAESTUS*: data analysis for X-ray absorption spectroscopy using *IFEFFIT***.** *J. Synchrotron Radiat.* **2005**, *12*, 537-541.

41. Gu, D.; Jia, C.-J.; Weidenthaler, C.; Bongard, H.-J.; Spliethoff, B.; Schmidt, W.; Schüth, F. Highly Ordered Mesoporous Cobalt-Containing Oxides: Structure, Catalytic Properties, and Active Sites in Oxidation of Carbon Monoxide. *J. Am. Chem. Soc.* **2015**, *137*, 11407 - 11418.

42. Carraro, F.; Vozniuk, O.; Calvillo, L.; Nodari, L.; La Fontaine, C.; Cavani, F.; Agnoli, S. In operando XAS investigation of reduction and oxidation processes in cobalt and iron mixed spinels during the chemical loop reforming of ethanol. J. Mater. Chem. A, **2017**, 5, 20808

43. Iwanowski, R. J.; Heinonen, M. H.; Janik, E. X-ray photoelectron spectra of zinc-blende MnTe. *Chem. Phys. Lett.* **2004**, *387*, 110 - 115.

44. Wang, H.; Yao, Q.; Wang, C.; Fan, B.; Sun, Q.; Jin, C.; Xiong, Y.; Chen, Y. A simple, one-step hydrothermal approach to durable and robust superparamagnetic, superhydrophobic and electromagnetic wave-absorbing wood. *Sci. Rep.* **2016**, *6*, 35549.

45. Lei, S.; Liu, L.; Wang, C.; Shen, X.; Wang, C.; Guo, D.; Zeng, S.; Cheng, B.; Xiao, Y.; Zhou, L. A facile *in situ* reduction route for preparation of spinel $CoCr_2O_4$ polycrystalline nanosheets and their magnetic properties. *CrysEngCommun.* **2014**, *16*, 277 - 286.

46. Shen, H.; Chen, J.; Dai, H.; Wang, L.; Hu, M.; Xia, Q. New Insights into the Sorption and Detoxification of Chromium(VI) by Tetraethylenepentamine Functionalized

Nanosized Magnetic Polymer Adsorbents: Mechanism and pH Effect. *Ind. Eng. Chem. Res.* **2013**, *52*, 12723 - 12732.

47. Zhang, X.; van den Bos, C.; Sloof, W. G.; Hovestad, A.; Terryn, H.; de Witt, J. W. H. Drying Effects on Corrosion Properties of Cr(VI)- and Cr(III)-Treated Electrogalvanized Steel. *ECS Trans.* **2006**, *1*, 165 - 176.

48. Hotchandani, S.; Ozdemir, U.; Allakhverdiev, S. I.; Karacan, N.; Klimov, V. V.; Kamat, P.V.; Carpentier, R. Redox characteristics of manganese and cobalt complexes obtained from pyridine N-oxide. *Bioelectrochemistry* **2000**, *51*, 175 - 180.

49. Solla-Gullón, J.; Vidal-Iglesias, F. J.; Herrero, E.; Feliu, J. M.; Aldaz, A. CO monolayer oxidation on semi-spherical and preferentially oriented (1 0 0) and (1 1 1) platinum nanoparticles. *Electrochem. Communi*. **2006**, *8*, 189 - 194.

50. Garcia. G.; Koper. M. T. M. Stripping voltammetry of carbon monoxide oxidation on stepped platinum single-crystal electrodes in alkaline solution. *Phys. Chem. Chem. Phys.*, **2008**, *10*, 3802 - 3811.

51. Schmidt, T. J.; Noeske, M.; Gasteiger, H.A.; Behm, R.J.; Britz, P.; Brijoux, W.; Bonnemann, H. Electrocatalytic Activity of PtRu Alloy Colloids for CO and CO/H_2Electrooxidation: Stripping Voltammetry and Rotating Disk Measurements. *Langmuir* **1997**, *13*, 2591 - 2595.

52. Ueda, A.; Yamada, Y.; Ioroi, T.; Fujiwara, N.; Yasuda,K.; Miyazaki, Y.; Kobayashi, T. Electrochemical oxidation of CO in sulfuric acid solution over Pt and PtRu catalysts modified with TaO_x and NbO_x. *Catal. Today* **2003**, *84*, 223 - 229.

Table 1. Physical properties like Elemental ratio, Crystallite sizes, BET surface area, Pore diameter, pore volumes in Co_3O_4 Spinel catalysts.

Catalysts	**Element ratio (ICP-AES)**	**Crystallite size (nm)**	**BET surface area ($m^2 g^{-1}$)**	**Pore Diameter (nm)**	**Pore Volume (cm^3/g)**
Co_3O_4	-	-	102.0	-	-
$MnCo_2O_4$	Mn:Co [1:1.94]	12	43.0	15.5	0.156
$MnFe_2O_4$	Mn:Fe [1:1.92]	12	49.4	8.2	0.103
$CoCr_2O_4$	Co:Cr[1:1.93]	17	100.0	5.1	0.128
$CoFe_2O_4$	-	-	53.5	9.2	0.123
$FeCr_2O_4$	-		127.4	4.3	0.139

Table 2. Bond distances and mean square radial disorder (MSRD) for different scattering correlations for tetrahedral and octahedral cations in Co_3O_4, $MnCo_2O_4$, $CoCr_2O_4$ and $MnFe_2O_4$.

Bond	**Coordination Number**	**Bond length (Å)**	**MSRD (σ^2) ($Å^2$)**
Co_3O_4			
Co K edge			
O	4	1.921(5)	0.0035(6)
Co(octa)	12	3.352(7)	0.0033(8)
Co(tetra)	4	3.46(2)	0.001(1)
O	6	1.910(5)	0.0035(6)
Co (octa)	6	2.858(4)	0.0032(4)
Co(tetra)	6	3.352(7)	0.0033(8)
$MnCo_2O_4$			
Co K edge			
O	4	1.914(4)	0.0037(6)
Mn/Co (octa)	12	3.376(7)	0.007 (1)
Co (tetra)	4	3.52(4)	0.010 (6)
O	6	1.914(4)	0.0037(6)
Co/Mn(octa)	6	2.860(4)	0.0031 (4)
Co (tetra)	6	3.376(7)	0.007 (1)
Mn K edge			
O (octa)	6	1.902(9)	0.004(1)
Mn/Co (octa)	6	2.89(1)	0.006(1)
Co (tetra)	6	3.39(1)	0.008(1)
$CoCr_2O_4$			
Co K edge			
O	4	1.96(1)	0.007(2)
Cr (octa)	12	3.41(1)	0.009(2)
Co (tetra)	4	3.54(3)	0.006(3)
Cr K edge			
O	6	2.004(7)	0.003(1)
Cr (octa)	6	2.998(8)	0.0042(8)
Co (tetra)	6	3.50(1)	0.009(2)
$MnFe_2O_4$			
Fe K edge			
O	4	1.92(1)	0.010(2)
Mn/Fe (octa)	12	3.44(2)	0.014 (2)
Fe (tetra)	4	3.75(9)	0.019 (13)
O	6	1.92(1)	0.010 (2)
Fe/Mn(octa)	6	2.97(1)	0.012 (2)
Fe (tetra)	6	3.44(2)	0.014 (2)
Mn K edge			
O (octa)	6	1.92(1)	0.007(2)
Mn/Fe (octa)	6	2.96(1)	0.011(2)
Fe (tetra)	6	3.43(2)	0.013(2)

Table 3: Binding energies (B.E.) (eV) of Mn, Co, Cr and Fe species in $MnCo_2O_4$, $CoCr_2O_4$, $MnFe_2O_4$, $CoFe_2O_4$, $FeCr_2O_4$, and CoO catalysts along with relative peak areas (%) given in bracket.

Catalysts	**Mn $2p_{3/2}$**	**Co $2p_{3/2}$**	**Cr $2p_{3/2}$**	**Fe $2p_{3/2}$**
$MnCo_2O_4$	Mn^{2+}: 640.8 (70%) Mn^{4+}: 643.1 (30%)	Co^{2+}: 781.8 (29%) Co^{3+}: 779.7 (71%)	–	–
$CoCr_2O_4$	Co^{2+}: 781.1 (100%)	–	Cr^{3+}: 576.2 (76%) Cr^{6+}: 578.7 (24%)	–
$MnFe_2O_4$	Mn^{2+}: 640.9 (56%) Mn^{4+}: 643.0 (44%)	–	–	Fe^{2+}: 709.5 (40%) Fe^{3+}: 711.5 (60%)
$CoFe_2O_4$	–	Co^{2+}: 781.4	–	Fe^{2+}: 709.3 (29%) Fe^{3+}: 711.4 (71%)
$FeCr_2O_4$	–	–	Cr^{3+}: 576.5	Fe^{2+}: 709.2 (40%) Fe^{3+}: 711.5 (60%)
CoO	–	Co^{2+}: 780.9 (100%)	–	–

Figures

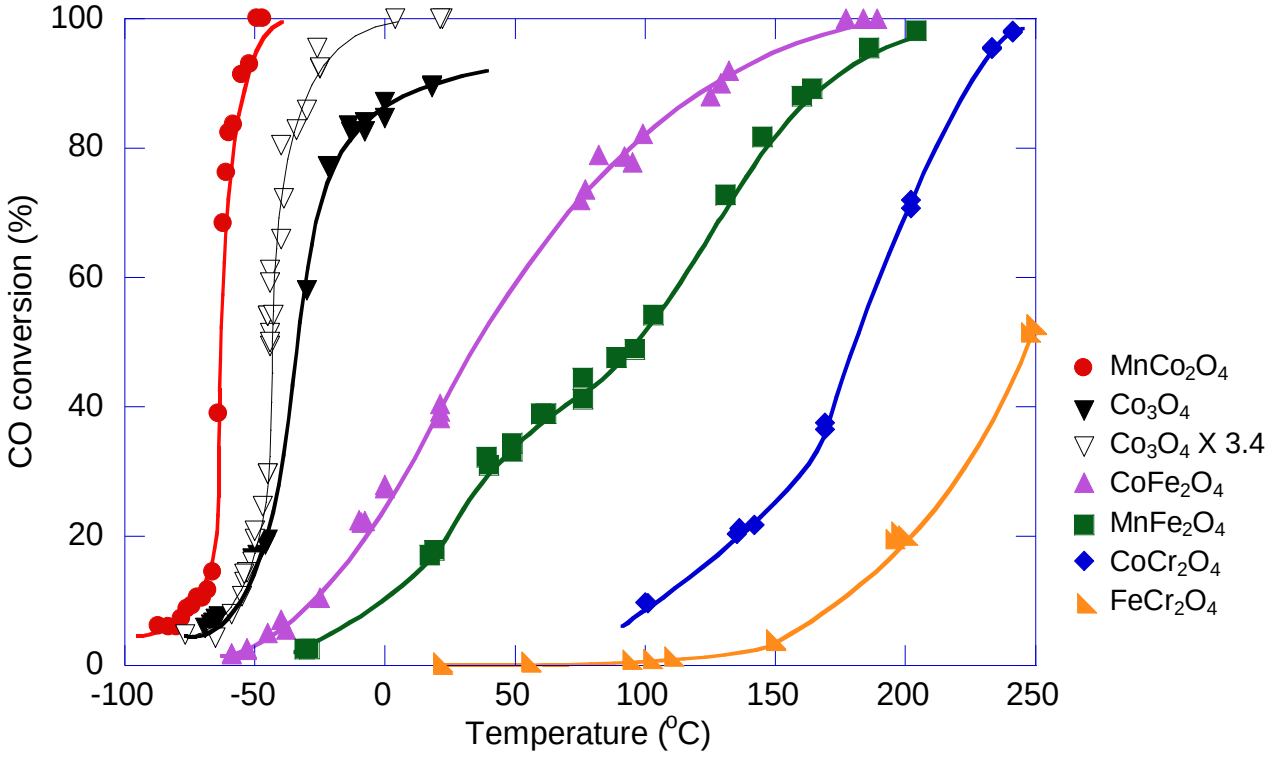

Figure 1. CO oxidation profiles with surface area normalized weight for various spinel based oxides

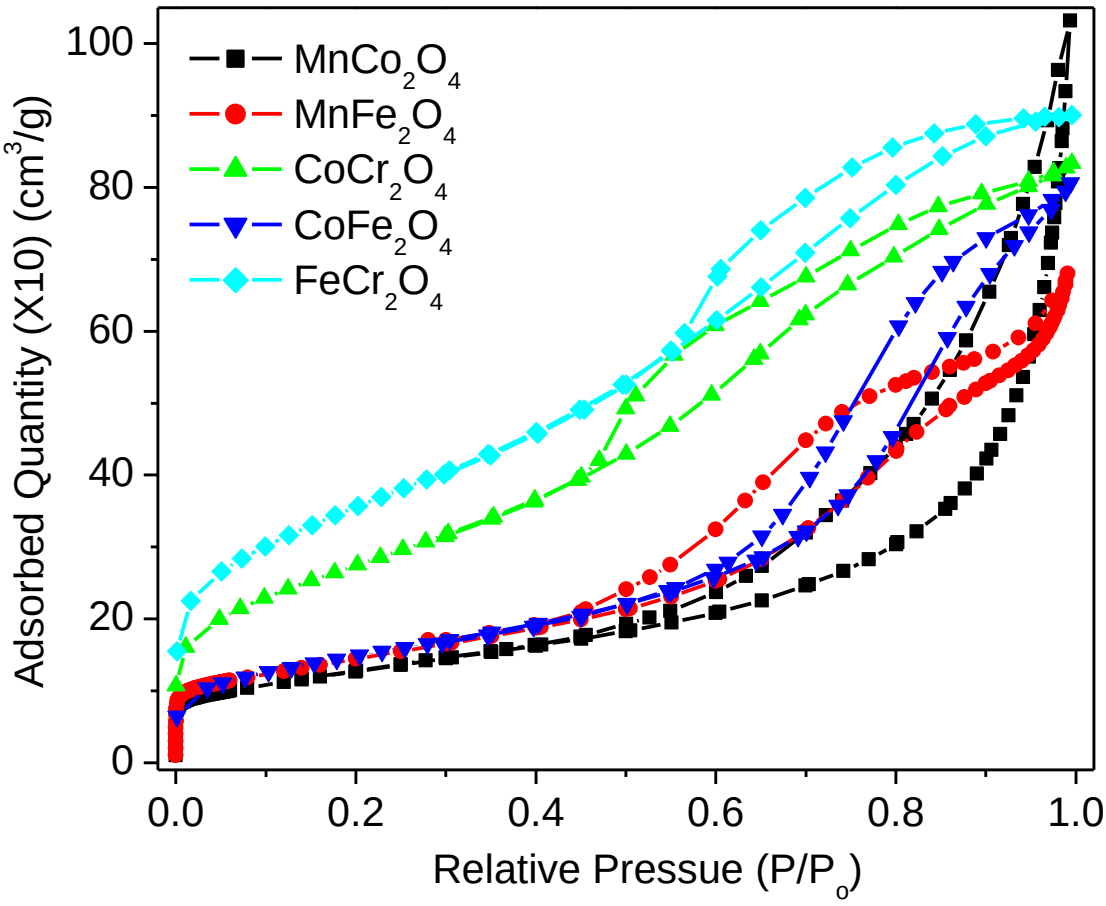

Figure 2. BET N_2 adsorption vs relative pressure (P/P_o) curves for all Co_3O_4 based catalysts

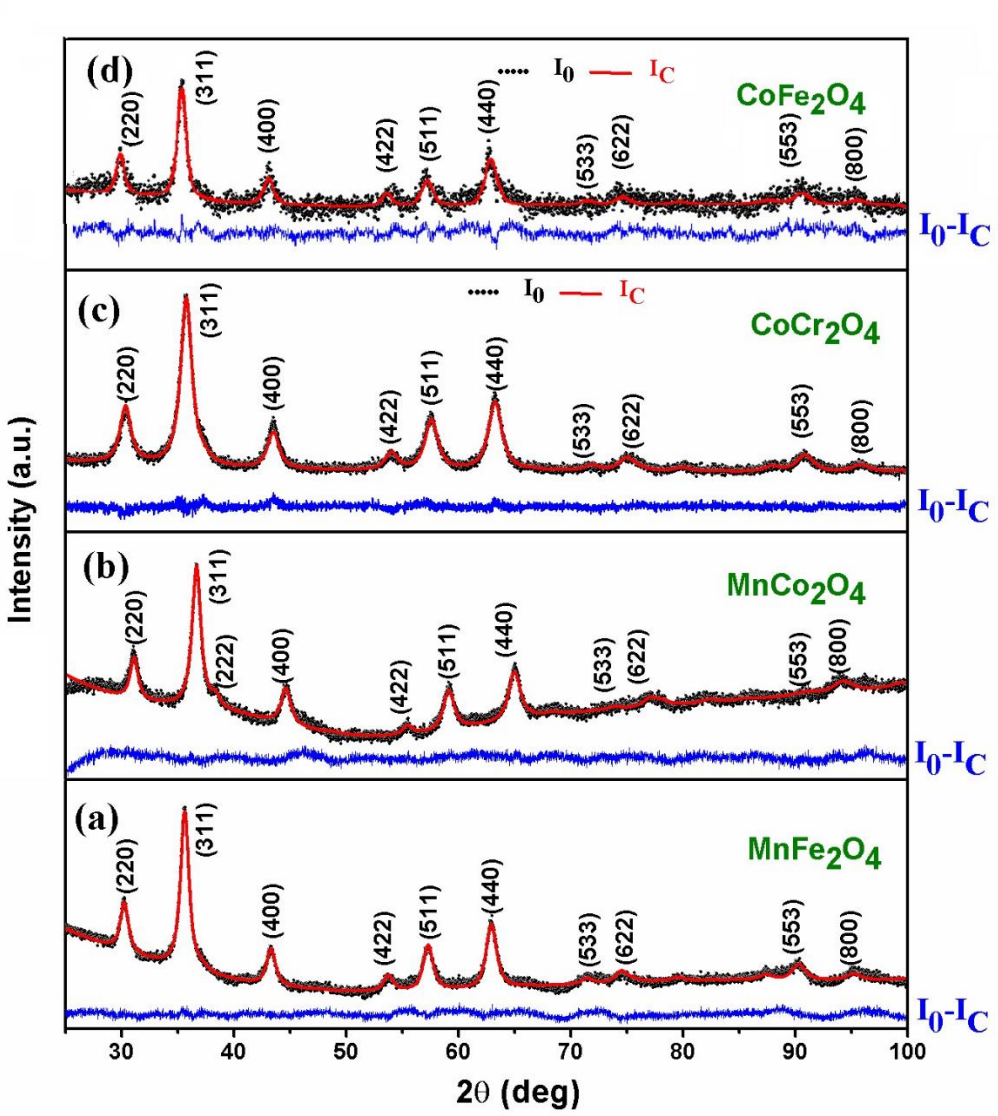

Figure 3: Rietveld analysis output profiles of (a) $MnFe_2O_4$, (b) $MnCo_2O_4$, (c) $CoCr_2O_4$ and (d) $CoFe_2O_4$ (I_o – Observed, I_c – Calculated, I_o-I_c is the difference).

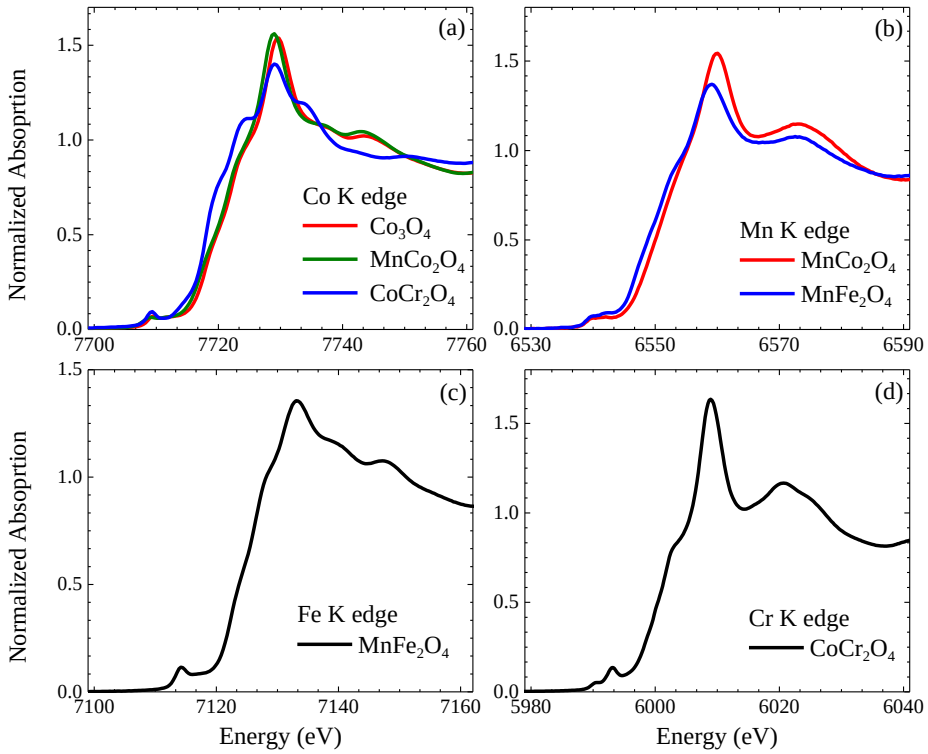

Figure 4. XANES spectra of various metal atoms in Co_3O_4, $MnCo_2O_4$, $MnFe_2O_4$ and $CoCr_2O_4$.

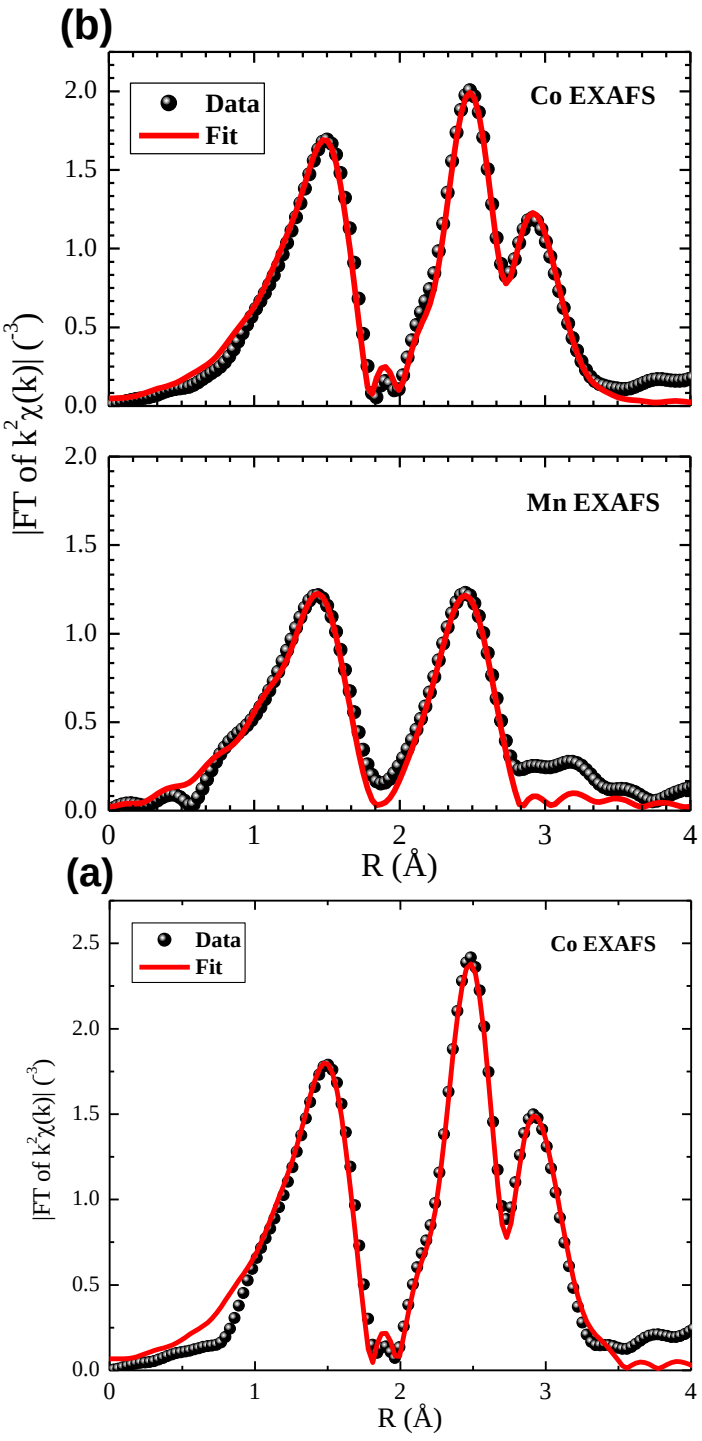

Figure 5. Magnitude of the FT of k^2 weighted EXAFS spectra vs radial distribution and fitted curve in (a) Co_3O_4 and (b) $MnCo_2O_4$.

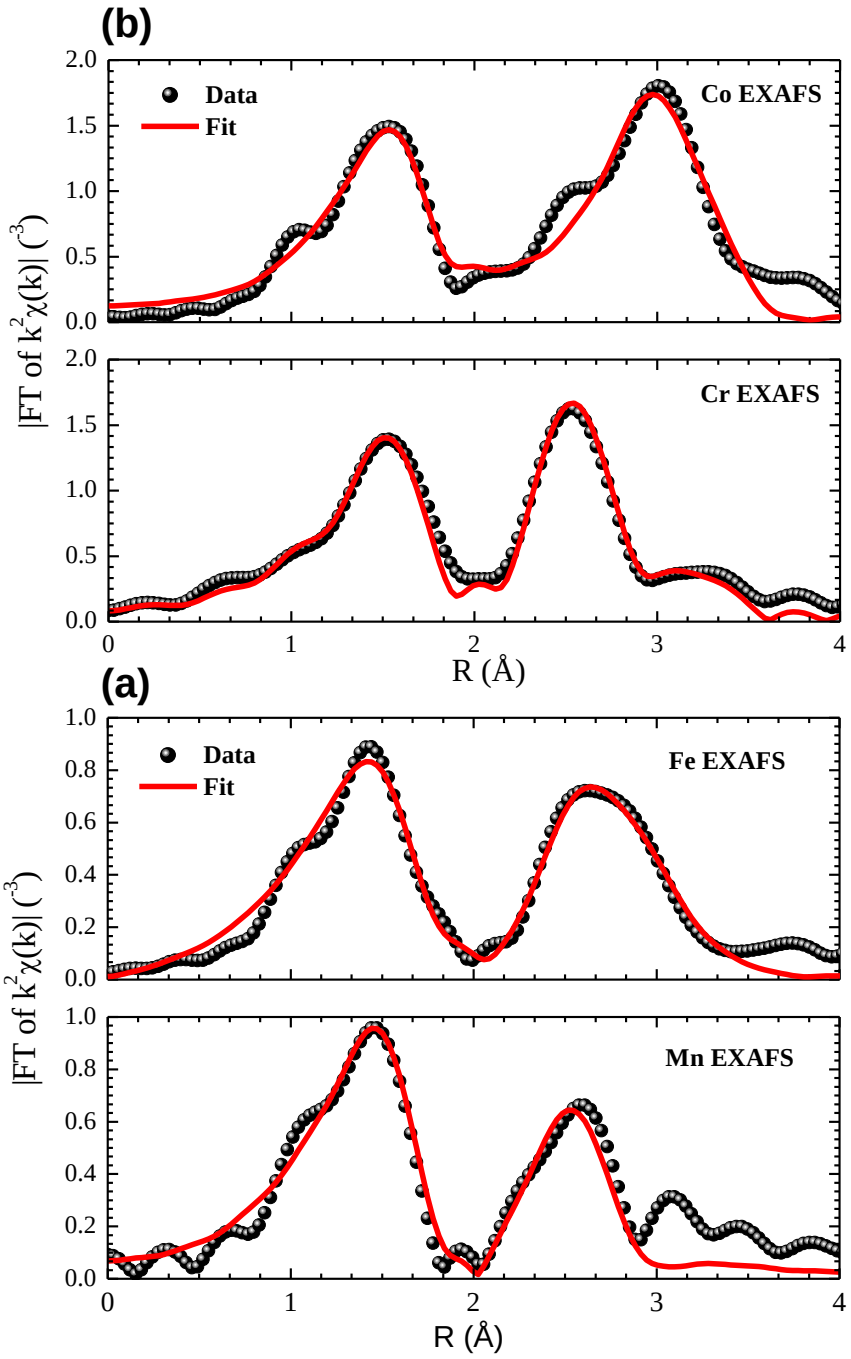

Figure 6. Magnitude of the FT of k^2 weighted EXAFS spectra vs radial distribution and fitted curve in (a) $MnFe_2O_4$ and (b) $CoCr_2O_4$.

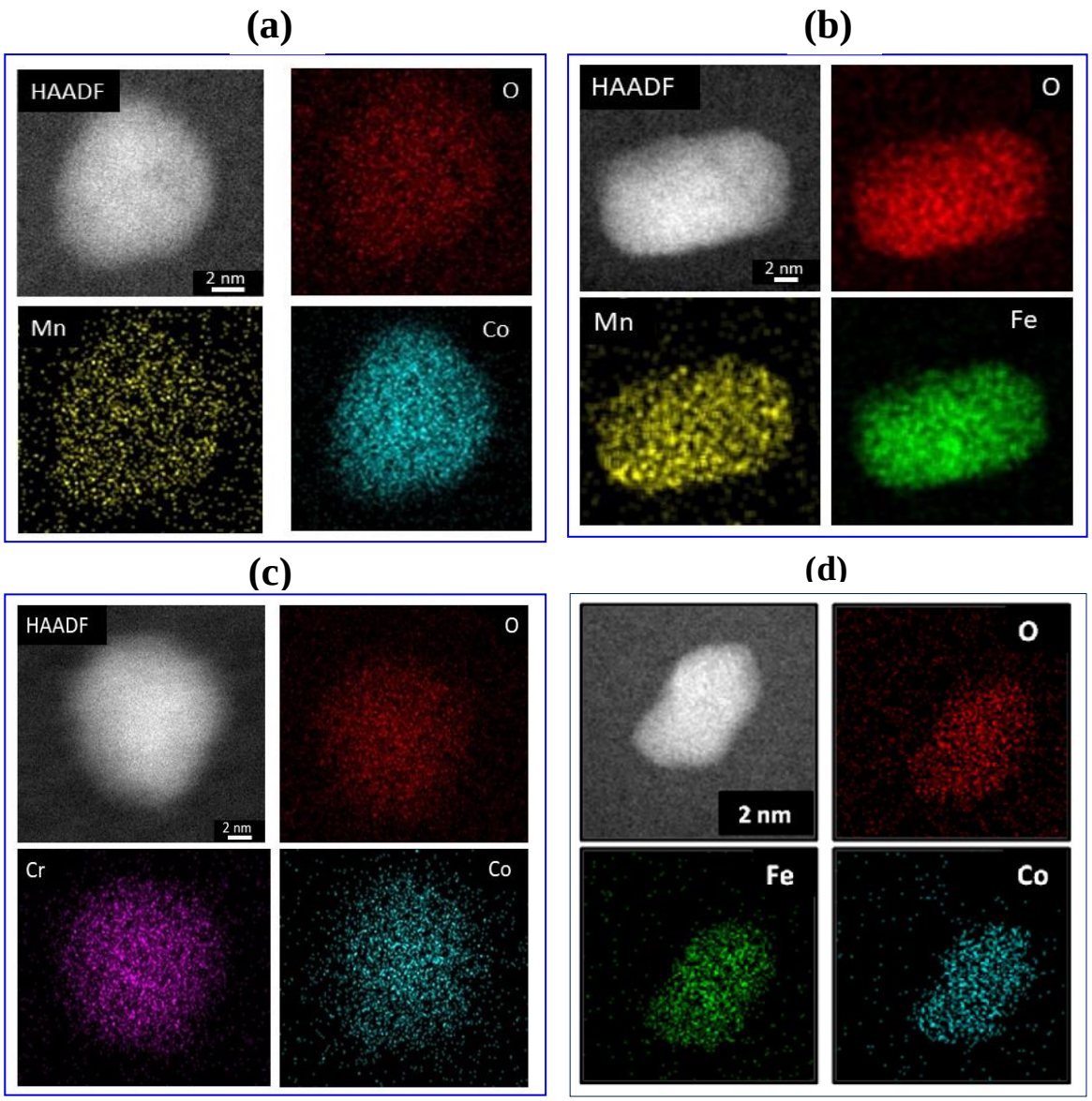

Figure 7. Elemental distributions mapping in (a) $MnCo_2O_4$, (b) $MnFe_2O_4$ (c) $CoCr_2O_4$, (d) $CoFe_2O_4$

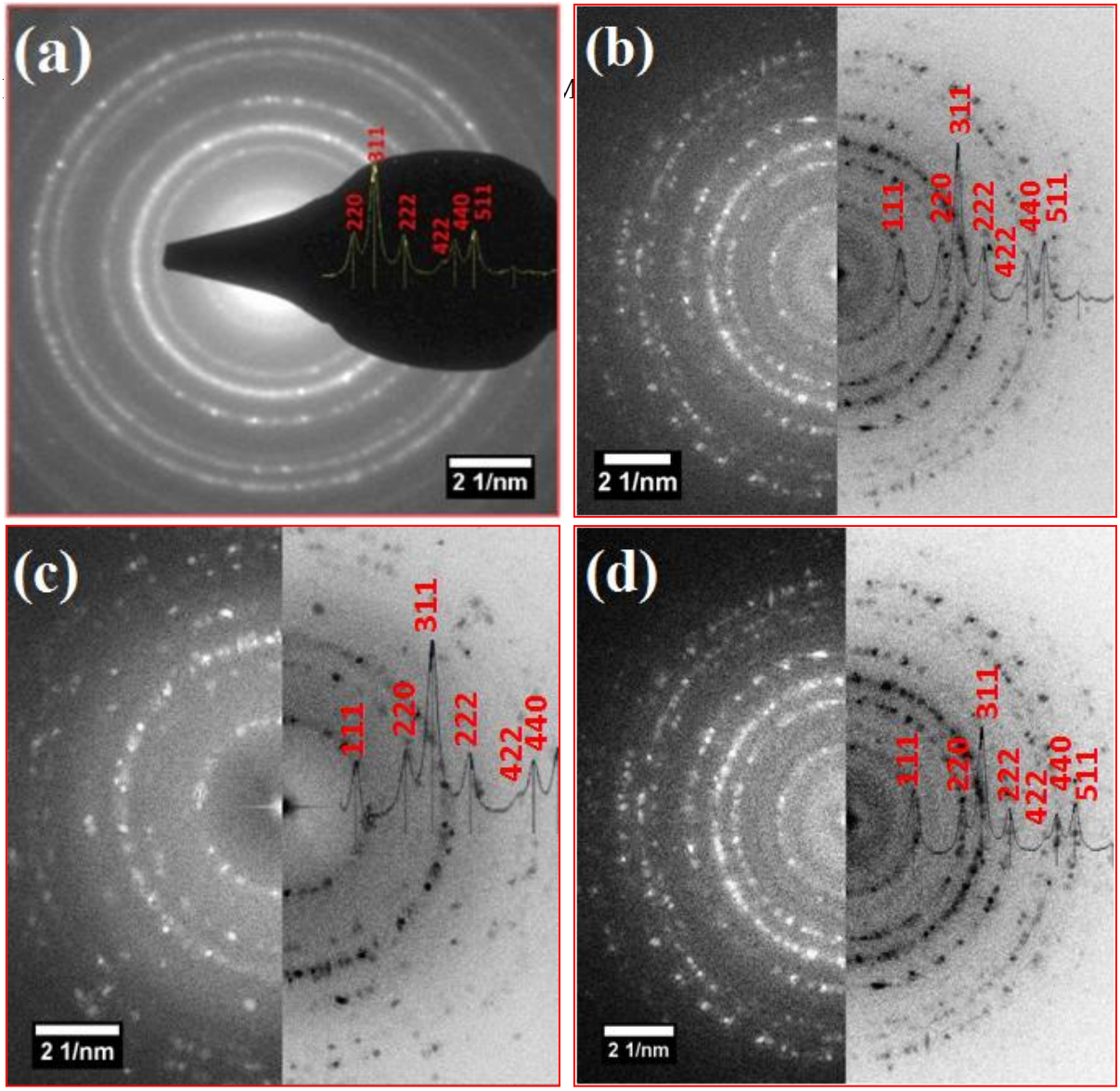

Figure 8. Electron Diffraction (ED) pattern in (a) $MnCo_2O_4$, (b) $MnFe_2O_4$ (c) $CoCr_2O_4$, (d) $CoFe_2O_4$

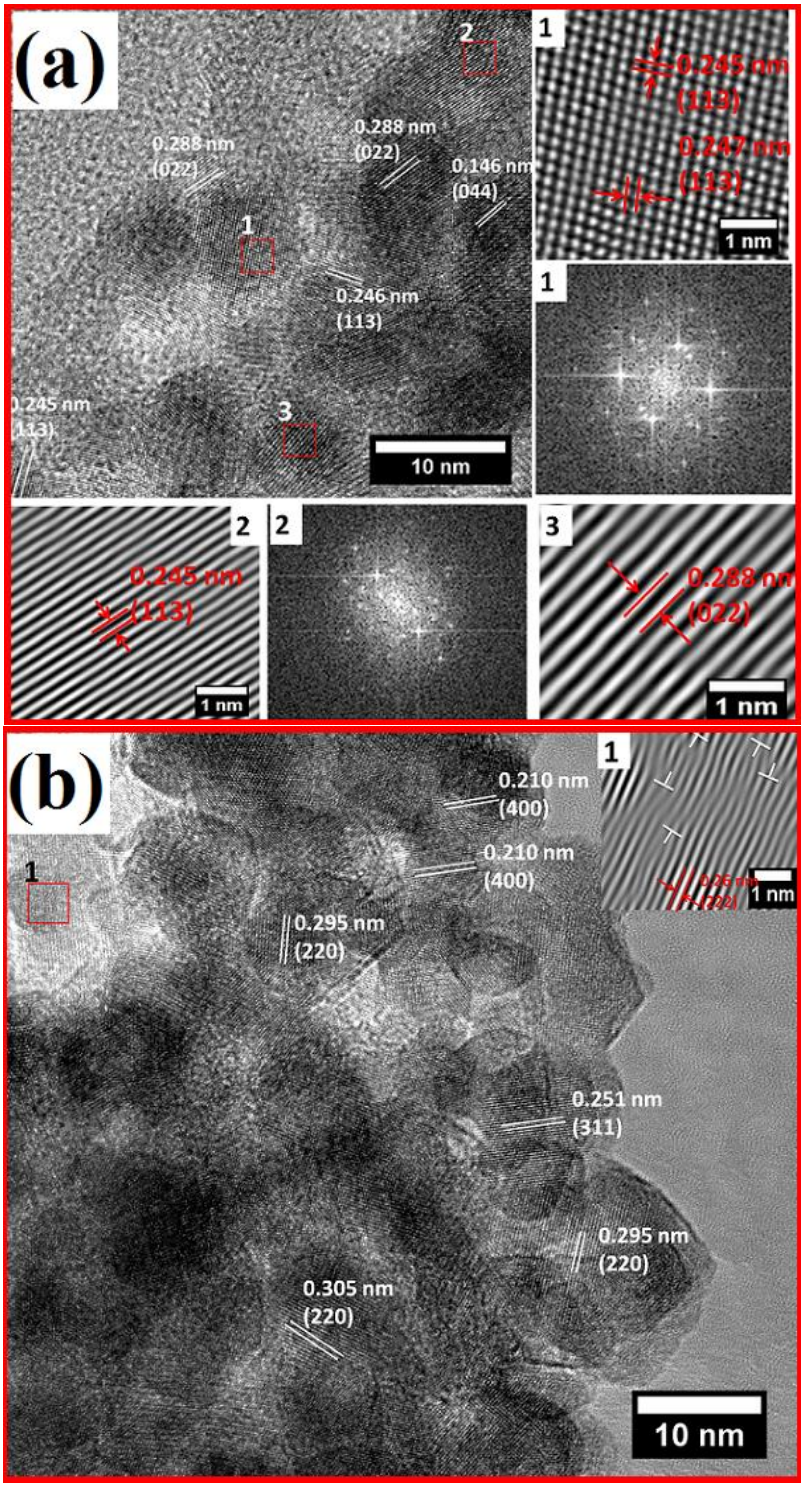

Figure 9. TEM images in $MnCo_2O_4$ (a) and $MnFe_2O_4$ (b) catalysts

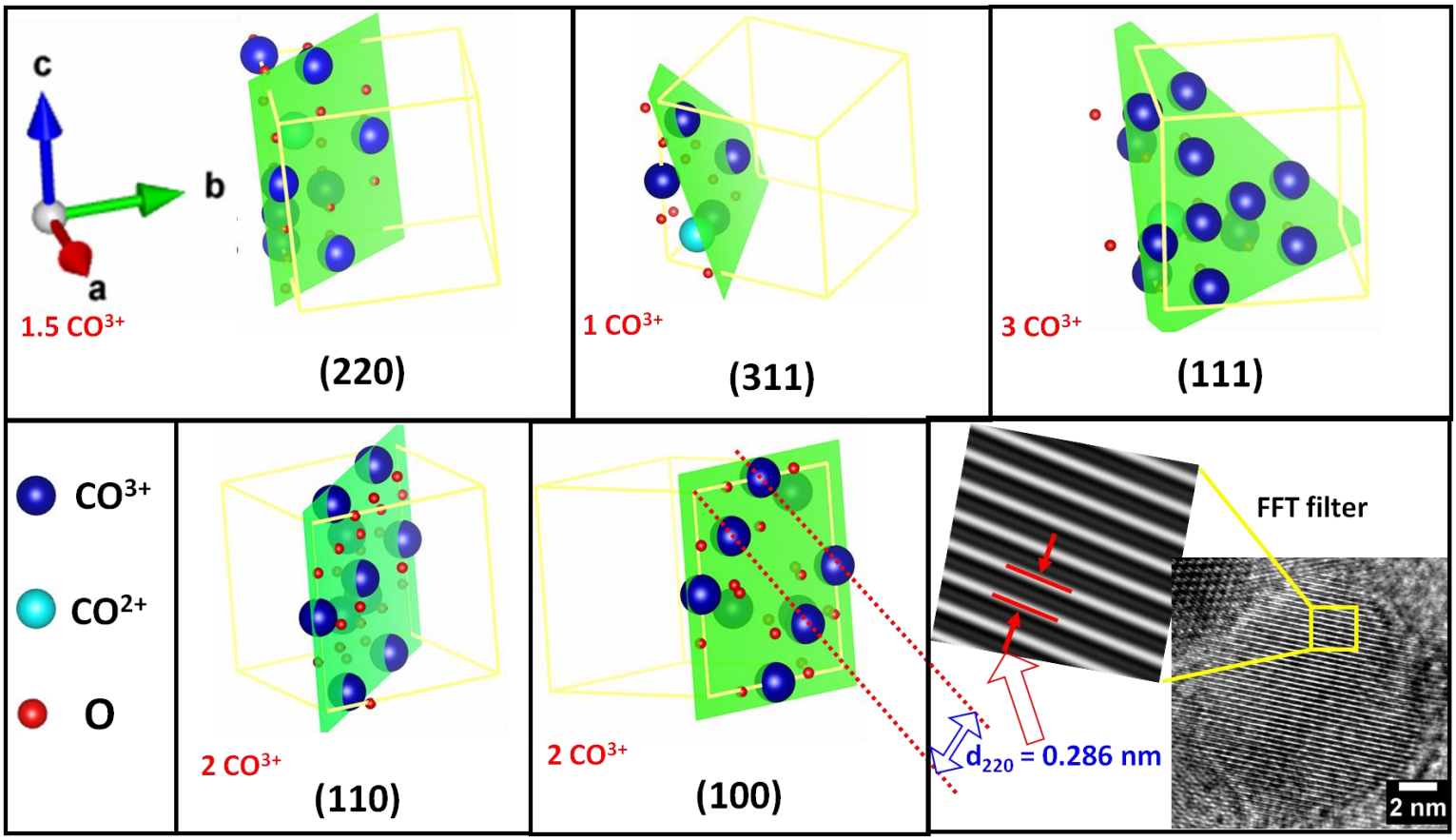

Figure 10. Different lattice planes with concentration of Co^{3+} species in Co_3O_4 based catalyst and a specimen of projected plane calculated from TEM.

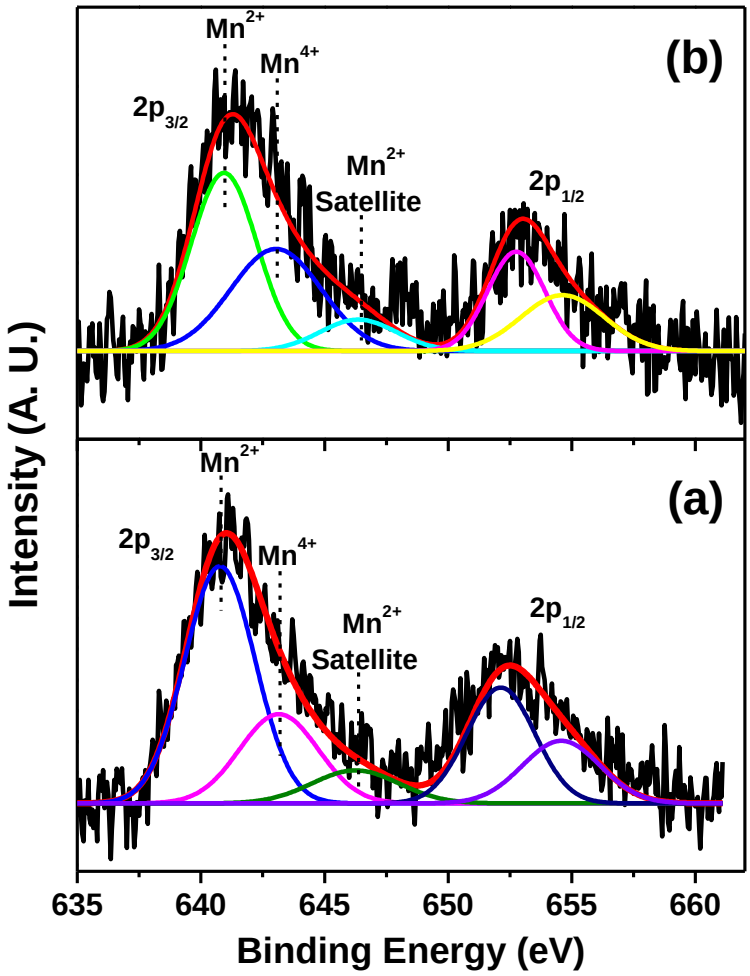

Figure 11. Mn(2p) core-level spectra in (a) $MnCo_2O_4$ and (b) $MnFe_2O_4$ catalysts

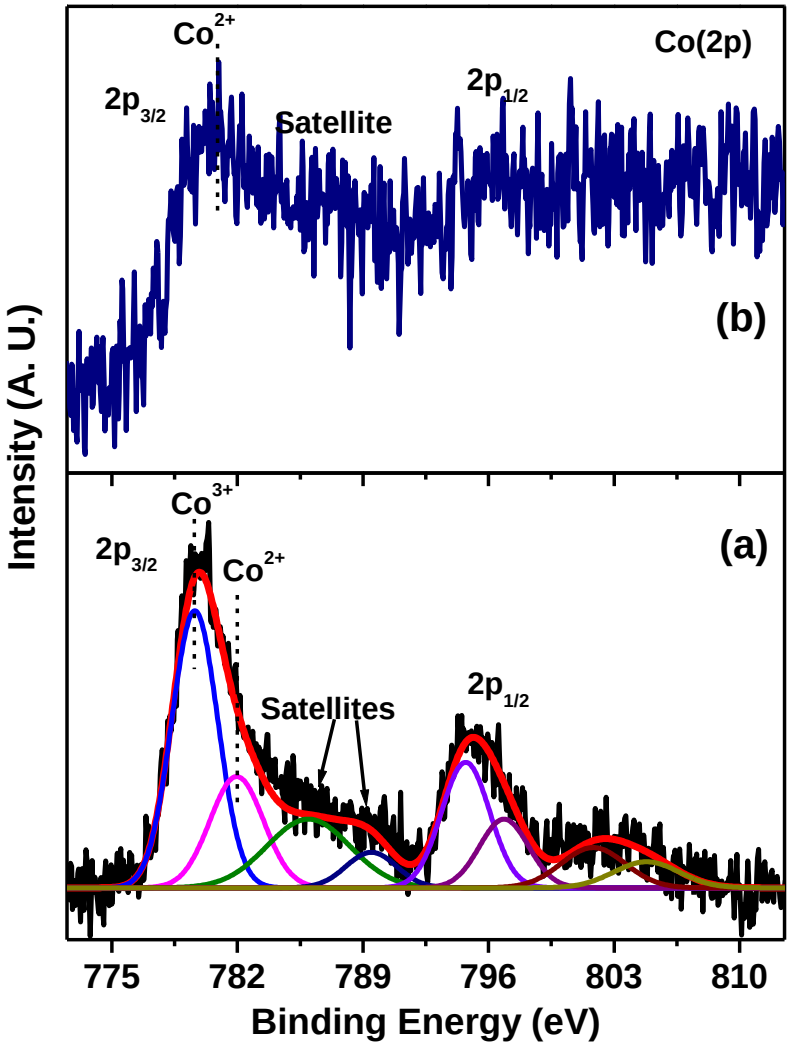

Figure 12. Co(2p) core-level spectra in (a) $MnCo_2O_4$ and (b) $CoCr_2O_4$ catalysts

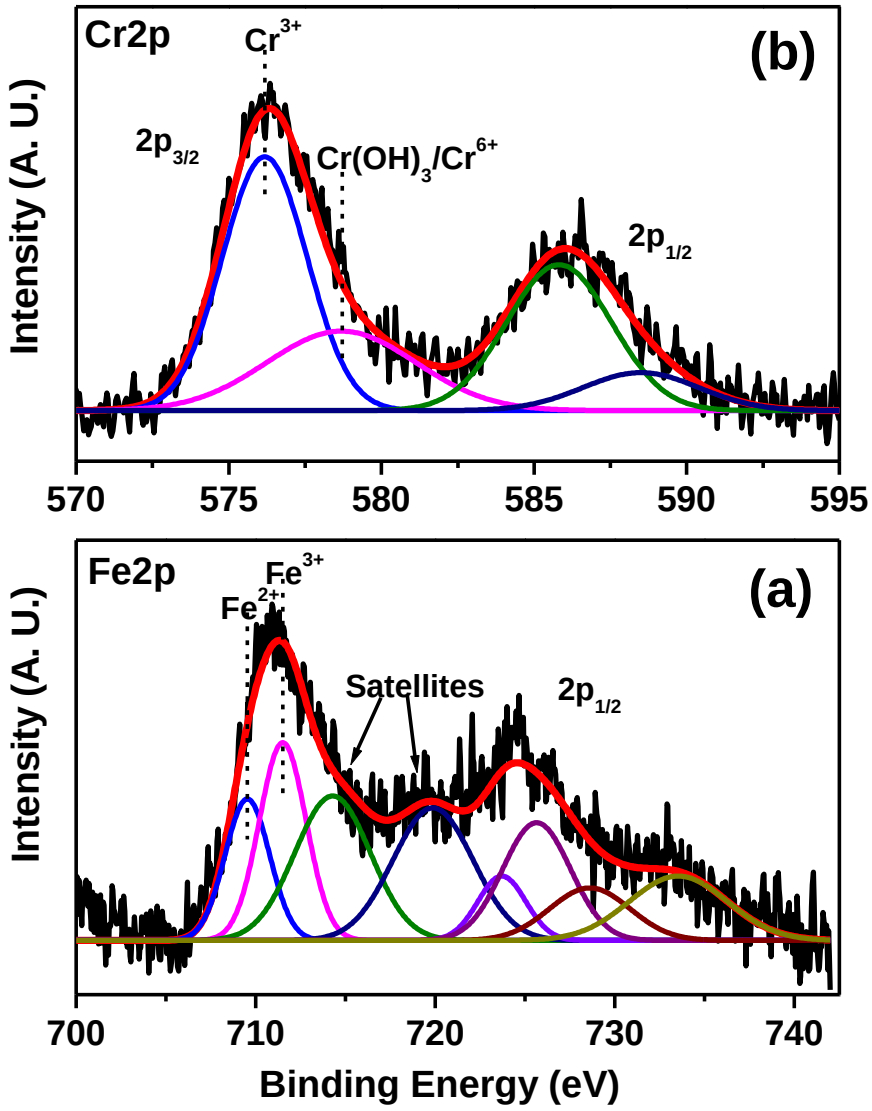

Figure 13. (a) Fe(2p) core-level spectra in $MnFe_2O_4$ catalyst ; (b) Cr(2p) core-level spectra in $CoCr_2O_4$ catalyst

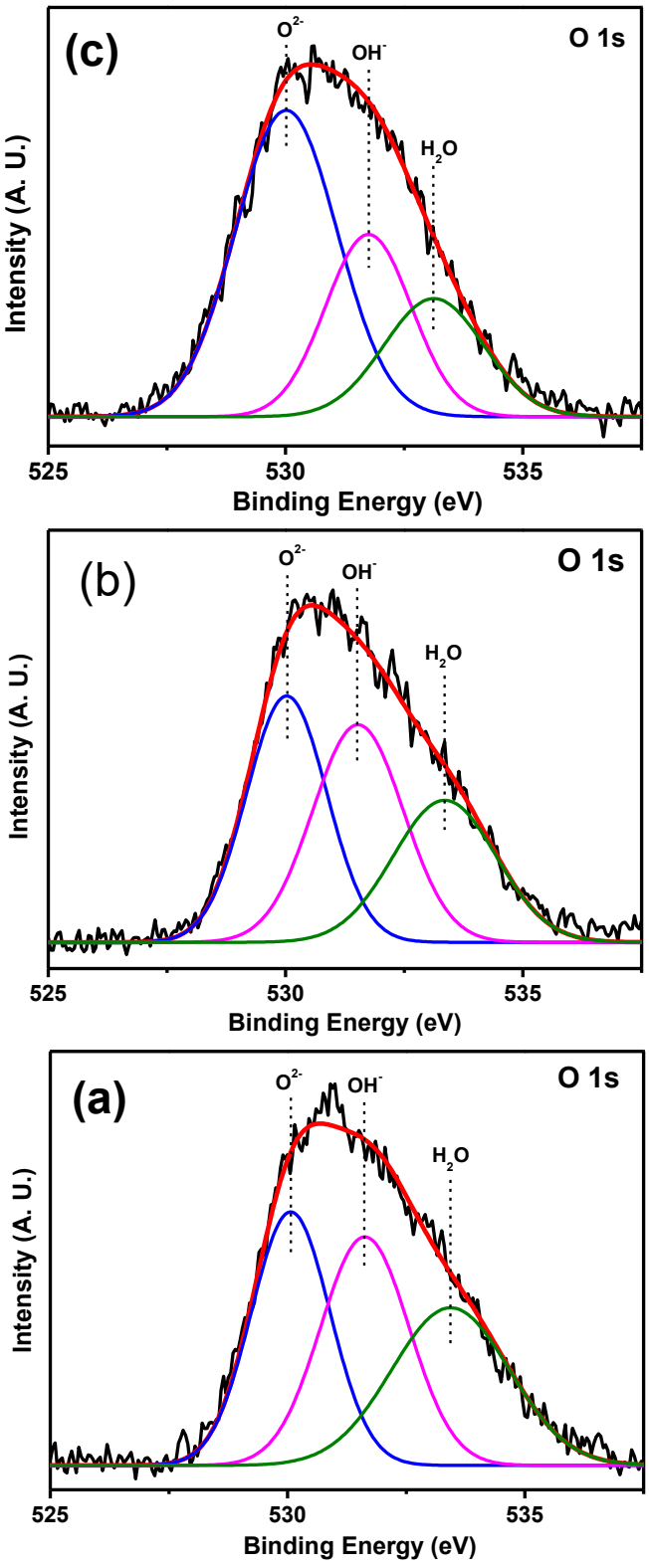

Figure 14. O(1s) core-level spectra in (a) $MnCo_2O_4$, (b) $MnFe_2O_4$ and (c) $CoCr_2O_4$ catalysts

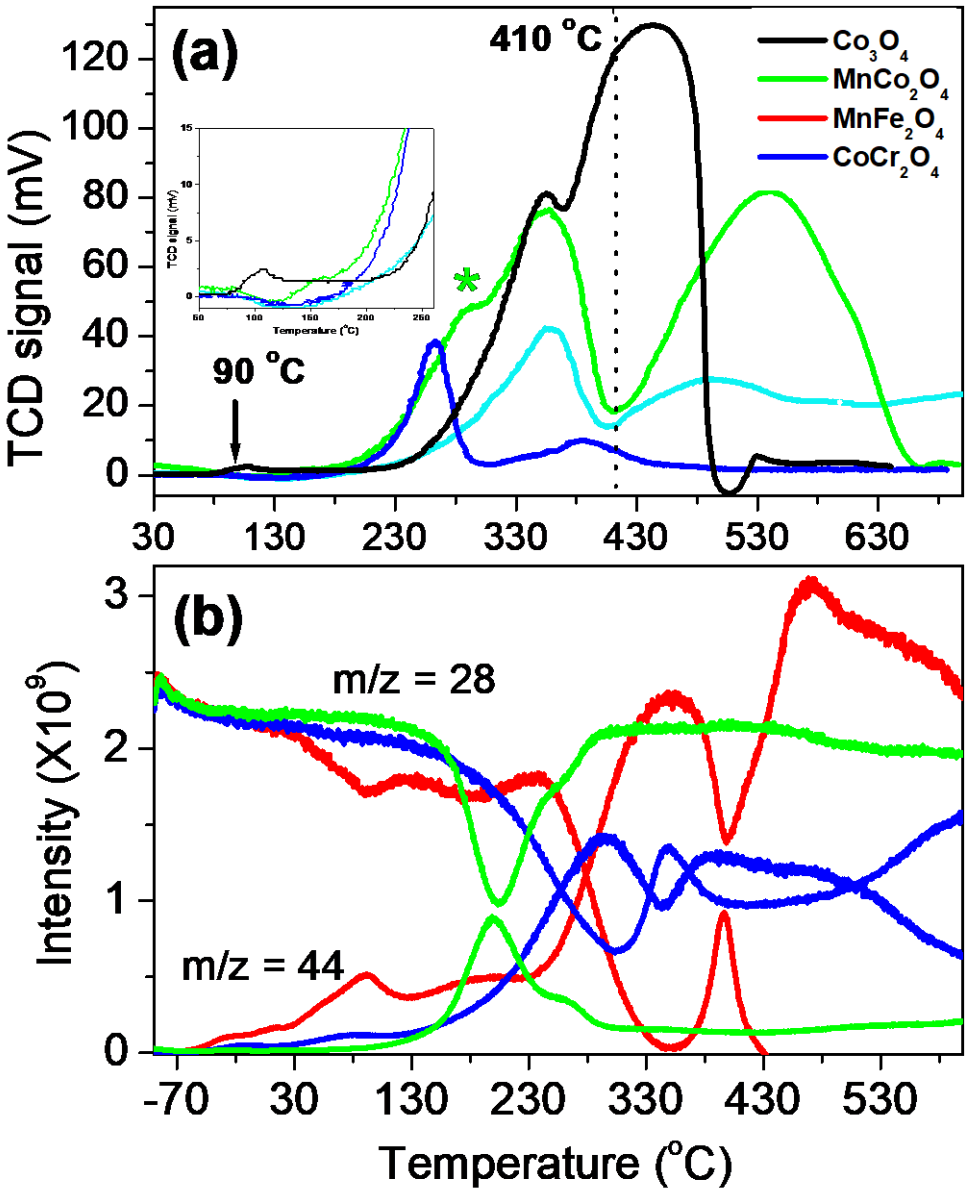

Figure 15. H_2 TPR (a) and CO TPR (b) in $MnCo_2O_4$, $MnFe_2O_4$ and $CoCr_2O_4$ catalysts (Color code same for same catalyst in both figures)

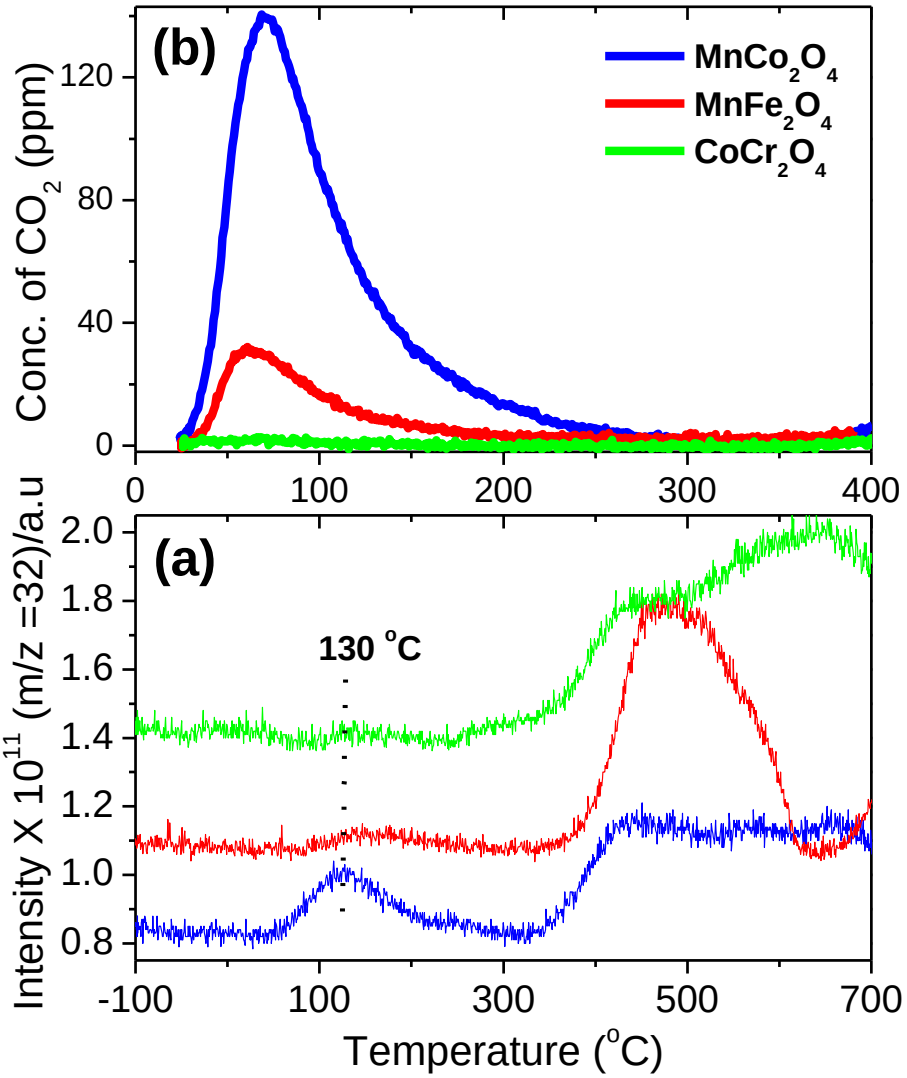

Figure 16. O_2 TPD (a) and CO_2 TPD (b) over $MnCo_2O_4$, $MnFe_2O_4$ and $CoCr_2O_4$ catalysts (Color code same in both figures)

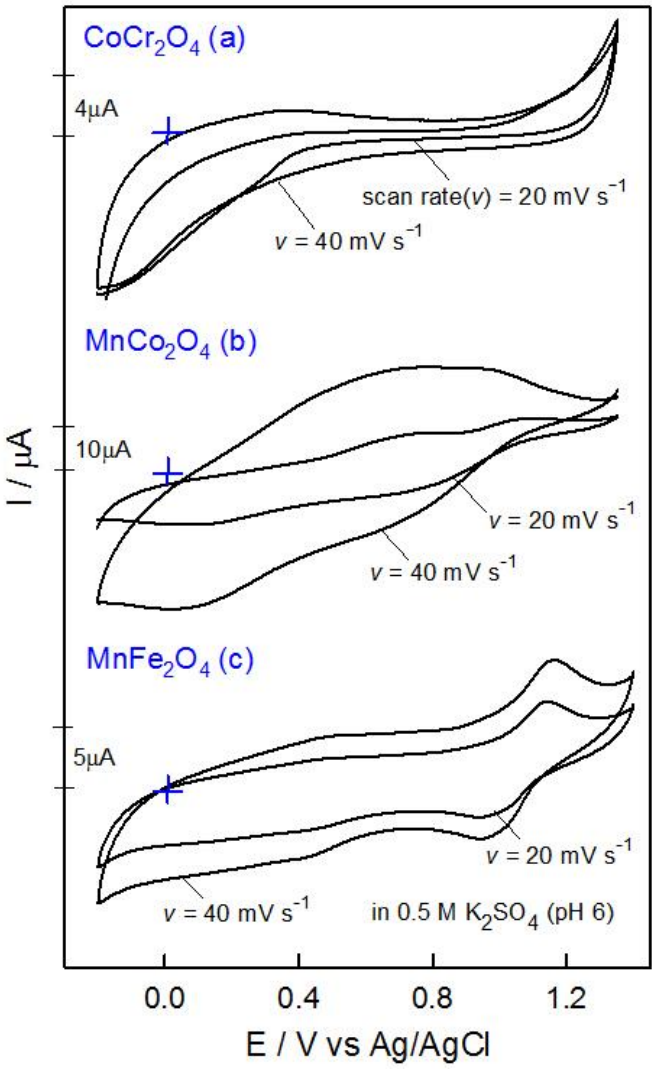

Figure 17: CV on $CoCr_2O_4$ (a), $MnCo_2O_4$ (b) and $MnFe_2O_4$ (c) in K_2SO_4 medium. The chosen potential range is -0.2 to 1.4 V. pH is kept at 6 and the scan rate is 40 mV s^{-1}.

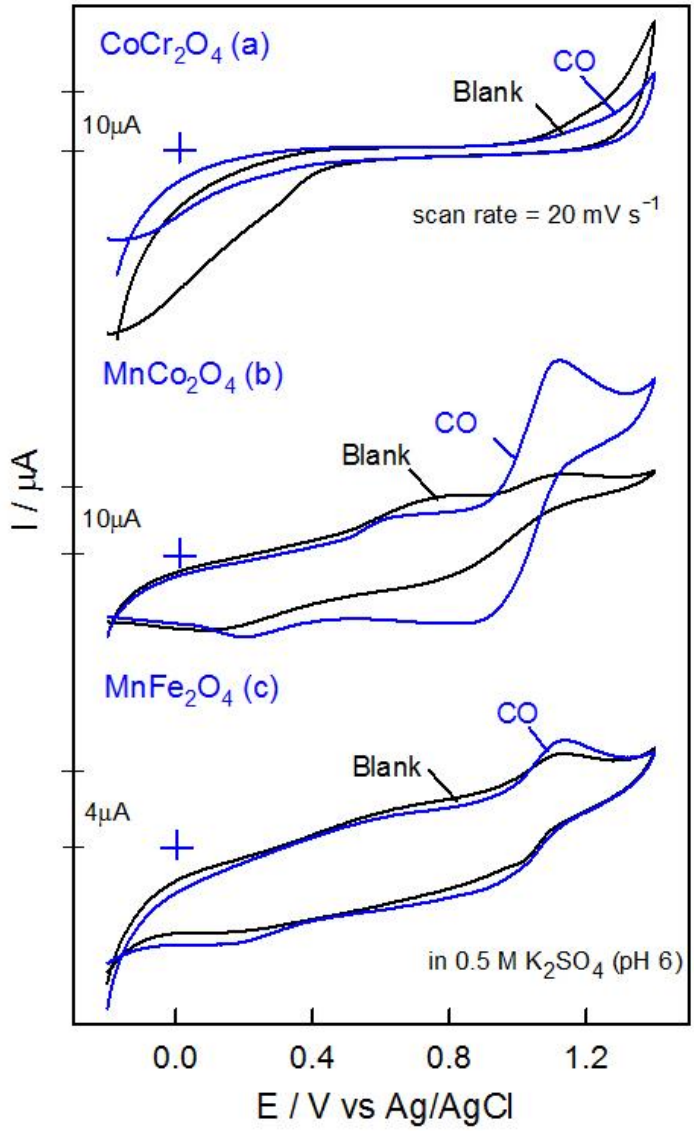

Figure 18: CV on $CoCr_2O_4$ (a), $MnCo_2O_4$ (b) and $MnFe_2O_4$ (c) in K_2SO_4 medium with and without CO. The chosen potential range is -0.2 to 1.4 V. pH is kept at 6 and the scan rate is 20 mV s^{-1}.

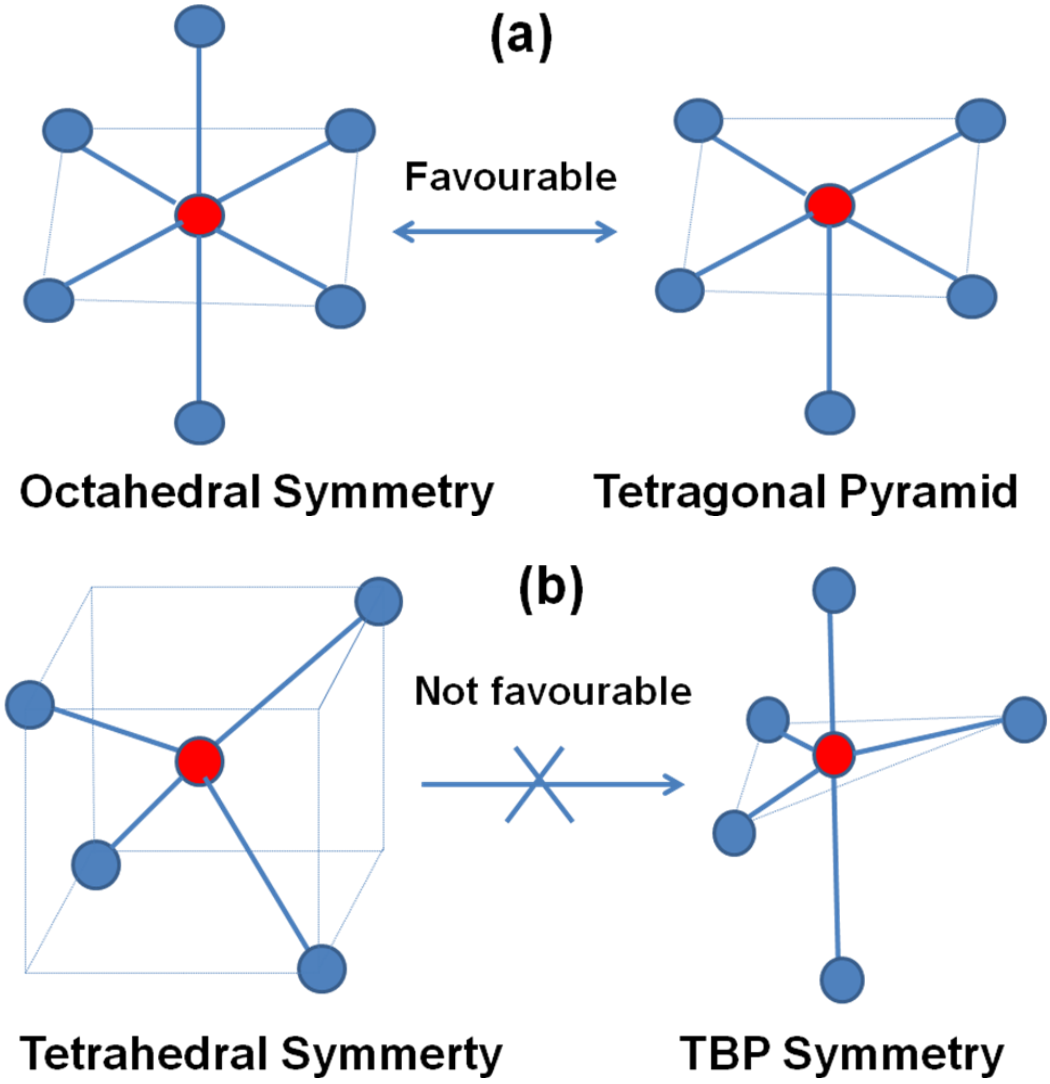

Figure 19. The probable symmetry change during redox reaction at tetrahedrally and octahedrally coordinated Cobalt atoms (Red ball – Cobalt ; Blue ball – Oxygen).

Supporting Informations:

Table S1: *Different structural and microstructural parameters of $MnFe_2O_4$, $MnCo_2O_4$ and $CoCr_2O_4$ spinel compounds as obtained from Rietveld refinement analysis.*

Sample	Crystal System & Sp.Gr.	Lattice Parameter (Å)	Atomic Positions	Fractional Coordinates			Crystallite Size (nm)	Lattice Strain
				x	y	z		
$MnFe_2O_4$	Cubic Fd-3m	8.3470	Mn^{2+}	0.125	0.125	0.125	12.63	0.002621
			Fe^{3+}	0.500	0.500	0.500		
			Fe^{3+}	0.125	0.125	0.125		
			O^{2-}	0.3712	0.3712	0.3712		
$MnCo_2O_4$	Cubic Fd-3m	8.1066	Mn^{2+}	0.125	0.125	0.125	11.35	0.001378
			Co^{3+}	0.500	0.500	0.500		
			Co^{3+}	0.125	0.125	0.125		
			O^{2-}	0.3644	0.3644	0.3644		
$CoCr_2O_4$	Cubic Fd-3m	8.3118	Co^{2+}	0.125	0.125	0.125	9.72	0.002981
			Cr^{3+}	0.500	0.500	0.500		
			Cr^{3+}	0.125	0.125	0.125		
			O^{2-}	0.3612	0.3612	0.3612		

Table S2. Binding energies, relative peak areas of different oxygen species of $MnCo_2O_4$, $MnFe_2O_4$ and $CoCr_2O_4$ catalysts evaluated from O 1s core level spectra

Catalysts	O species	O 1s binding energy (eV)	Relative peak area (%)
$MnCo_2O_4$	O^{2-}	530.1	34
	OH^-	531.6	34
	H_2O	533.4	32
$MnFe_2O_4$	O^{2-}	530.0	36.5
	OH^-	531.5	36.5
	H_2O	533.4	27
$CoCr_2O_4$	O^{2-}	530.0	53
	OH^-	531.7	27
	H_2O	533.1	20

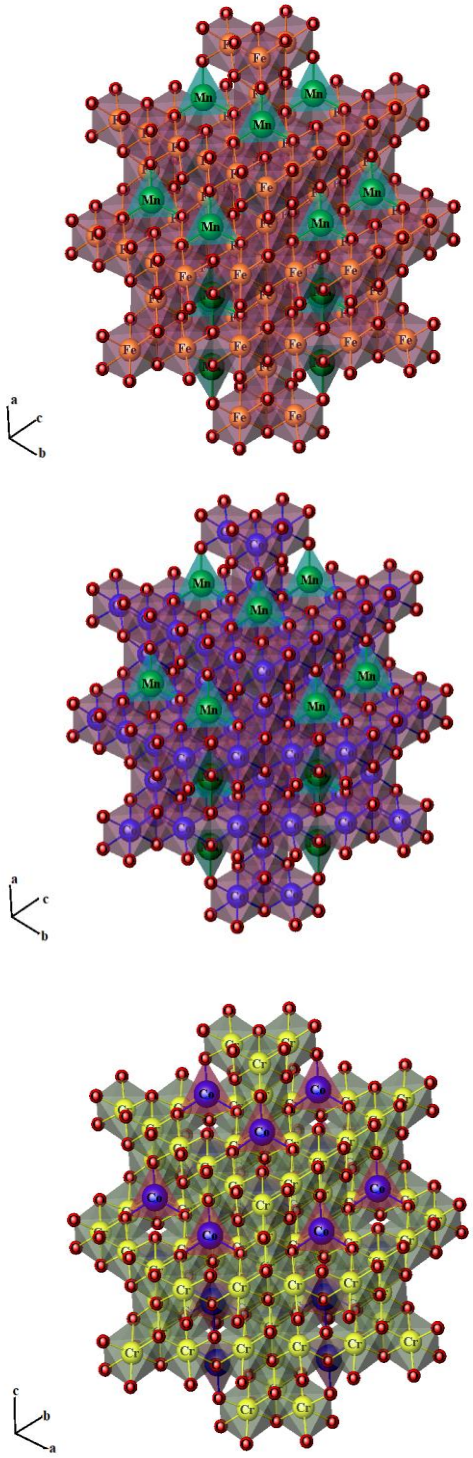

Figure S1. Spinel structure of (a) $MnFe_2O_4$, (b) $MnCo_2O_4$, and (c) $CoCr_2O_4$

Above figure shows the atomic coordinate sites occupied by various metals like Mn, Fe, Co and Cr in Co_3O_4 based spinel structure.

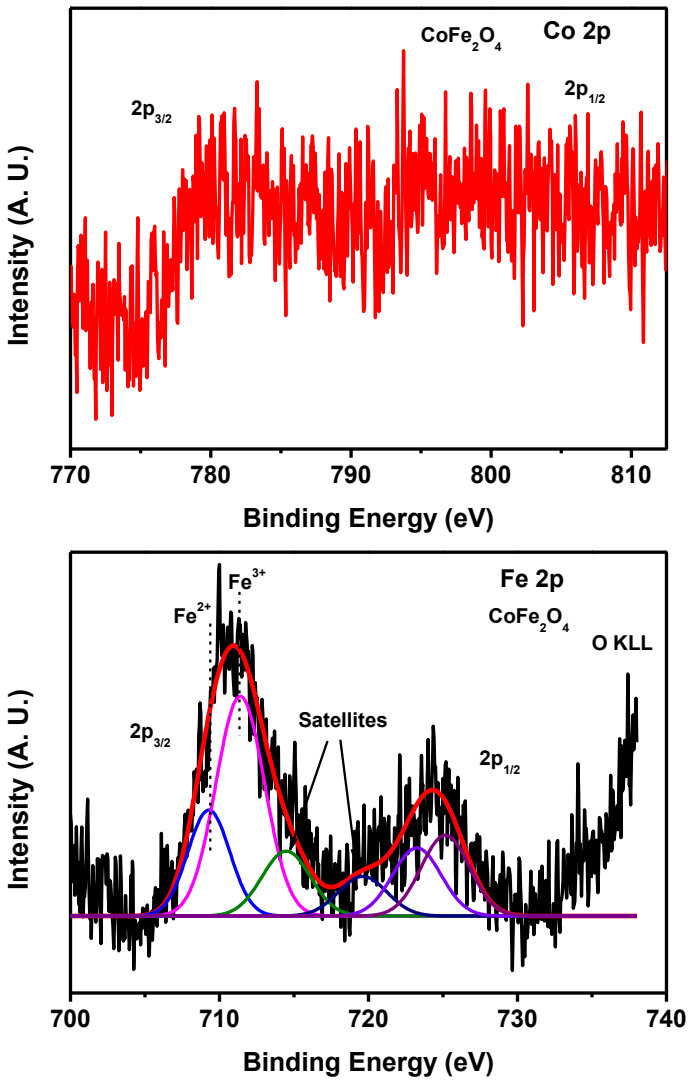

Figure S2. XPS of Co 2p and Fe 2p in $CoFe_2O_4$ catalyst.

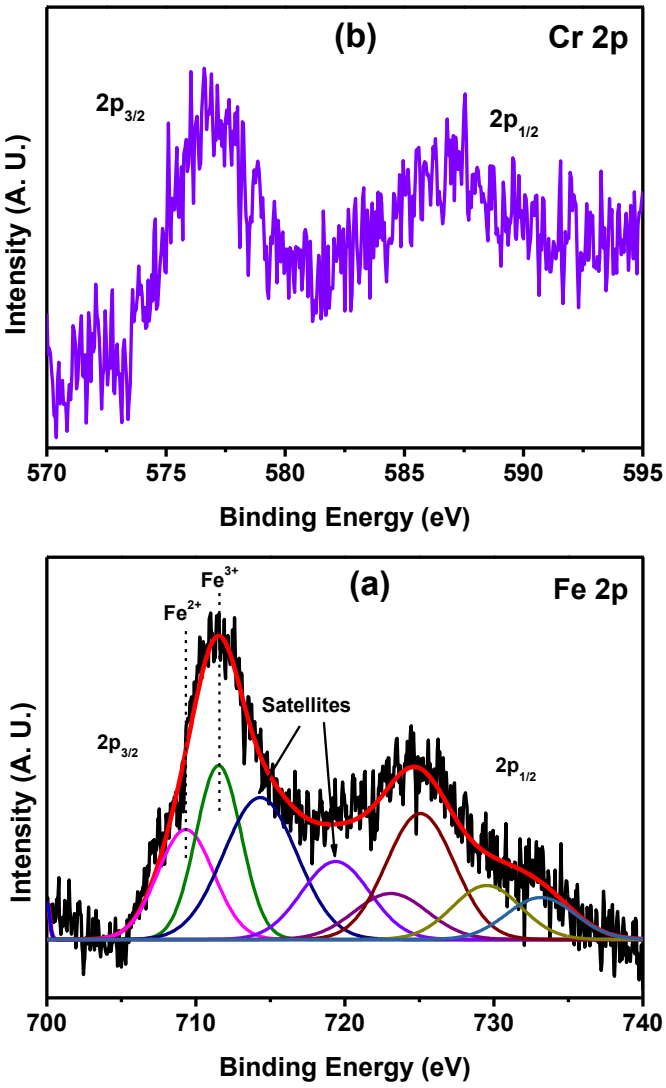

Figure S3. XPS of Fe 2p and Cr 2p in $FeCr_2O_4$ catalyst.